Three-Dimensional Quantitative Thermal Mapping
of the Human Body

Tze-Yuan Cheng, Srikamal Kandala, and Cila Herman

Department of Mechanical Engineering, Johns Hopkins University,

3400 N. Charles Street, Baltimore, MD, USA 21218-2682

Abstract

Infrared (IR) thermography is a non-invasive imaging modality that allows the measurement of the spatial/temporal variations of the infrared radiation emitted by the human body and captured by the two-dimensional (2D) focal plane array of the IR camera. The challenge in quantitative medical diagnostic applications is the need to convert the radiation emitted by the complex, three-dimensional (3D) shape of the human body into accurate temperature data. Errors based on the 2D information captured by the 2D focal plane array of the camera, using calibration algorithms provided by the manufacturer, can be of the order of 2-4°C. Temperature resolution of the order of 0.1°C or better is desired in quantitative medical diagnostic applications. The magnitude of the temperature measurement error strongly depends on the orientation of the surface relative to the camera axis. The aim of this study is to develop methodologies that will accurately map temperature distribution on 3D skin surfaces captured using 2D thermography and acquired by the IR camera. Therefore, we devised a method to generate 3D IR thermographic data using the Microsoft Kinect imager along with appropriate software tools coupled with a precision 2D IR imager. An algorithm was developed to map the 2D IR radiation information captured by a sensitive, high-resolution 2D infrared imager onto the 3D shape data captured by Kinect. Furthermore, an approach which takes into account the viewing angle distribution over the 3D surface is proposed to compensate for the IR imaging artifact caused by the directional property of the emissivity. The devised methodology reported in this paper successfully demonstrated the feasibility of mapping the 2D IR thermography data into the 3D body surface data. The accuracy of temperature measurement was improved by applying a correction formula to account for the directional properties of emissivity. The achieved accuracy of the resulting 3D temperature texture on skin surface reported in the study is promising for future clinical diagnostic applications of IR imaging.

Keywords: Quantitative infrared imaging, 3D medical thermography, 3D infrared thermography, 3D thermal mapping, Microsoft Kinect, 3D imaging, structure light projector, directional emissivity, viewing angle.

Abbreviations:

IR – infrared

2D – two dimensional

3D – three dimensional

List of symbols:

$T(\degree C)$ Temperature data measured by infrared camera (unit: degree Celsius)

g 2D pixel intensity of IR image for temperature conversion

X, Y, Z 3D world coordinates in pinhole model

x_c, y_c, z_c 3D camera coordinates in pinhole model

u, v 2D pixel coordinates in pinhole model

u_{0c}, v_{0c} Principal point (the center of 2D image coordinate)

T Transformation matrix from 3D world coordinates to 3D camera coordinates

R Rotation matrix in T

t Translation vector in T

f Focal length

α Pixel aspect ratio of 2D pixel coordinates

$[x_u, y_u]^T$ Liner projection on 2D image plane

$[x_d, y_d]^T$ The distorted projection on 2D image plane

$k_c = [k_1, k_2, k_3, k_4, k_5]$ Distortion coefficients of camera

$[u_d, v_d]^T$ Distorted pixel coordinates

x_d 3D coordinates with respect to the depth camera of Kinect

x_c 3D coordinates with respect to the color (RGB) camera of Kinect

x_i 3D coordinates with respect to infrared camera

$^D_C T$ Transformation matrix from the depth camera to the color camera of Kinect

$^D_C R$ Rotation matrix from the depth camera to the color camera of Kinect

$^D_C t$ Translation vector from the depth camera to the color camera of Kinect

$^C_I T$ Transformation matrix from the color camera of Kinect to infrared camera

$^C_I R$ Rotation matrix from the color camera of Kinect to infrared camera

$^C_I t$ Translation vector from the color camera of Kinect to infrared camera

θ Viewing angle with respect to surface normal

$\varepsilon(\theta)$ Directional emissivity at viewing angle θ

$\rho(\theta)$ Reflectivity at viewing angle θ

$\rho_\parallel(\theta)$ Parallel component of reflectivity

$\rho_\perp(\theta)$ Perpendicular component of reflectivity

$\boldsymbol{n_s}$	Index of refraction of skin
n_s	Real component of index of refraction of skin
k_s	Attenuation coefficient of skin
$\boldsymbol{n_a}$	Index of refraction of air
n_a	Index of refraction of air
β	Derived quantity used in the dielectric model of emissivity
p	Derived quantity used in the non-dielectric model of emissivity
q	Derived quantity used in the non-dielectric model of emissivity
λ	Wavelength in infrared spectrum
n_λ	Real component of index of refraction of pure water at wavelength λ
k_λ	Attenuation coefficient of pure water at wavelength λ
ΔT^c	Dimensionless temperature decay detected in IR image
T_s	Actual temperature of material surface
$T(\theta)$	Detected temperature in the IR image at viewing angle θ
ΔT	The differences between actual temperature T_s and detected temperature $T(\theta)$
T_a	Ambient temperature in IR imaging environment
T_0	Detected temperature $T(\theta)$ at the location with viewing angle $\theta = 0$
T_s^0	Estimated actual temperature at the location of zero viewing angle, obtained from the fir step of correction algorithm
S	Scaling factor derived from the ratio between T_s^0 and T_0, obtained in the second step of correction algorithm
$T_s^*(\theta)$	Actual temperature calibrated using scaling factor S, obtained in the third step of correction algorithm

1. Introduction and background

Thermoregulation is a physiological mechanism that maintains the temperature of the human body within specific, relatively narrow, boundaries. It responds to changes in the ambient and other external and internal variations (caused by disease, physical activity, mechanical or chemical stress and other factors) by controlling the rates of heat generation and heat loss. There is a large body of evidence that disease or deviation from normal function is accompanied by changes of body temperature, which again affect the temperature of the body surface (skin). For example, the behavior and appearance of some benign and cancerous lesions [1-9] and other inflammatory [10-12] processes differ from those of healthy tissue in terms of heat generation, because of a combination of inflammation, increased metabolic rate, interstitial hypertension, abnormal vessel morphology and lack of response to homeostatic signals.

The human body is a complex biophysical system because numerous parameters affect the temperature distribution within the body: understanding, modeling, and controlling these has been a quest since the early days of medicine. Clearly, accurate data about the temperature of the human body and skin, in addition to shape and color information, would be invaluable for a better understanding and diagnosing of the many complex processes. This information can be coupled with a high fidelity thermal (computational) model of the body to provide a wealth of information on the processes responsible for heat generation and thermoregulation, in particular the deviation from normal conditions that can be caused by disease, for diagnostic purposes as well as for the planning of treatment strategies.

Medical thermometers provide local estimates of the core body temperature. However, accurate temperature measurements of the human body, especially 3D temperature mapping of the skin temperature still remain a challenge. Body surface temperature and surface temperature in general are difficult to measure accurately using conventional sensors, since applying the sensor to the skin can in itself change the surface temperature distribution. Attempts with thermochromatic liquid crystals did not lead to quantitative diagnostic tools because of difficulties related to the application of the sensor, its influence on the temperature distribution of the surface to which it is applied and calibration issues. While researchers have been attempting to develop thermographic techniques (thermocromatic crystals, infrared thermography) for diagnostic applications for over four decades, they faced numerous challenges associated with the complexity of the investigated geometry, variations of surface properties and complexities of the imaging hardware.

Infrared (IR) thermography is a non-invasive imaging modality that allows the measurement of the spatial and temporal variations of the electromagnetic radiation emitted in the IR region of the spectrum by the object under study, which is the human body in this study. The emitted radiation and the skin surface temperature that can be derived from the emitted radiation data carry a wealth of information about different processes within the human body. The medical community embraced infrared imaging with enthusiasm in the sixties and attempts of quantitative diagnostic efforts were reported over the following two decades [9, 10, 13]. Following the initial enthusiasm interest waned, as early results did not meet expectations, due to insufficient temperature measurement accuracy, insufficient spatial resolution, lack of thorough insight into the underlying thermal processes, lack of adequate control of measurement and ambient conditions, complexity of implementation and equipment size, as well as cost [14]. Even though over the past four decades a considerable amount of effort focused on using IR imaging in medical diagnostics, the accurate quantification of skin temperature distributions

based on IR emission measurements remained an elusive task. Until recently, infrared imaging was mainly used as a research tool to gain additional qualitative insight into the temperature patterns of the skin, and its value in medical diagnostics was limited.

One of the rare FDA approved applications of IR thermography, breast cancer imaging, is qualitative [11, 15] and it is not widely used because early studies indicated that thermography yields too many false positive diagnoses of breast cancer. However, a longitudinal follow-up study of breast cancer patients conducted by Handley [16] in 1962 showed that the patients with 3 $^{\circ}$C temperature rise were more likely to present cancer in the future than those with only 1-2 $^{\circ}$C temperature rise. In 1980, Gautherie and Gros conducted another longitudinal study with a group of 1245 females [17] who had an abnormal IR image, but appeared to be normal under the conventional testing methods, including physical exam, mammography, ultrasound, and biopsy. They reported that within the subsequent five years, more than one third of the group with abnormal thermographic findings was diagnosed with breast cancer histologically. These two studies suggest that IR thermography holds potential to serve as a quantitative predictor, and it is also more sensitive than the conventional methods to detect early stage breast cancer.

Infrared imaging has experienced a revival and a revolution over the past 15 years as a result of the development of new materials used in focal plane arrays, new cooling methods that replaced cooling with liquid nitrogen and the introduction of novel uncooled detectors. This dramatic technology development was accompanied by the decrease of the cost of IR imaging systems since 2005. As a consequence, IR imagers that can yield high accuracy and high spatial and temporal resolution data have become available at a reasonable price. These developments were accompanied by the rapid progress in computer technology as well as the advances in computer vision algorithms since the 1990s, enabling novel and sophisticated applications. While military applications rely heavily on these new developments, progress is not yet reflected in medical applications. The research described in this study is a step in that direction.

IR thermography can be implemented either as a static or a dynamic technique in medical diagnostic applications. In static IR imaging, a steady state situation is measured: the patient is generally in thermal equilibrium, with normal ambient conditions present. The spatial distribution of thermal radiation emitted by the body is acquired and analyzed. In contrast, dynamic IR imaging detects both spatial and temporal variations of the emitted thermal radiation. Prior to image acquisition, a thermal excitation, such as cooling or heating, is applied to skin surface in dynamic IR imaging [8]. The phase after removal of thermal excitation is called thermal recovery process, during which IR images are acquired and analyzed. Dynamic imaging increases local temperature differences between healthy and diseased tissue, which yields a stronger signal essential in quantitative diagnostic applications. By analyzing thermal recovery of skin temperature, abnormalities such as malignancy of skin lesions can be examined, quantified and potentially diagnosed (with appropriate calibration and clinical validation) [1-8].

Several factors hindered widespread use of infrared thermography in quantitative medical diagnostic applications. The prevailing conception in part of the community is that the color coded images generated by commercial, off-the-shelf, often low-cost imagers deliver accurate temperature data for diagnostic applications, and that all problems with thermographic measurements have been resolved. Unfortunately, this is not the case, and there are numerous challenges in the development of quantitative diagnostic applications that need to be resolved first. For example, the data shown in the image generated by the imager can carry a variation up to 2-4°C, depending on surface shape, size and curvature, surface properties and ambient

conditions. This discrepancy can be explained by the calibration method using data for a blackbody, a flat surface with the emissivity of 1 perpendicular to the camera axis during the calibration process. While the skin emissivity is close to one, the temperature of the surfaces oriented away from the camera axes will appear lower because of the directional properties of the emissivity. The measurement error will increase with increasing angle and can reach several degrees. Therefore, one of the challenges in relating the infrared radiation emitted by the body and captured by the IR camera to temperature is the complex, three-dimensional (3D) shape of the body. The IR radiation captured by the focal plane array of the camera is affected by the geometry (shape and curvature), distance, skin surface properties, ambient conditions and the properties of the camera. Temperature resolution of the order of $0.1^{\circ}C$ or better is desired in quantitative medical diagnostic applications, therefore an error of this magnitude is unacceptable. In order to correct for the error caused by curvature effects, 3D data describing the shape of the imaged surface are required. This challenge is addressed in the research effort described in this paper: the aim is to develop methodologies that will accurately map temperature distributions on 3D surfaces.

Due to directional properties of emissivity, curved surfaces at constant temperature (such as the skin) will exhibit apparent temperature variations in IR thermography on portions of the surface with larger viewing angles. Based on the dielectric interface model, Watmough et al. [18] showed that the temperature drop due to this artifact is significant when the viewing angle is greater than 65°. The reflected radiation was taken into account in the study by Clark [19], and it showed that the measurement errors due to this artifact are likely to be proportional to the temperature difference between the skin surface and the environment. The reflected radiation is then included in the dielectric interface model by Martin and Watmough [20], which leads to a better agreement between the theoretical model and experimental data. The subsequent in-vivo measurement studies [20-23] showed the effective emissivity reduction due to this artifact in the wavelength range of 2-5 μm could be neglected when the viewing angle is smaller than 45°. The measurement errors increases dramatically - reaching 2.0 -3.0°C beyond this critical angle [20]. In 1992, based on the non-dielectric interface assumption, Hejazi and Spangler [24] developed a theoretical model of reflectivity and emissivity for human skin in the infrared wavelength range. The model provides an important basis to quantify the viewing angle artifact for skin in IR thermography. In view of the improved sensitivity of modern IR cameras, the temperature measurement accuracy requirements for diagnostic purpose have become more rigorous: $0.1^{\circ}C$ or better is desired for the detection of skin cancer [1-8, 25-27]. Thus, the correction for viewing angle artifact is crucial toward the accurate quantitative diagnosis based on IR thermography standardization. To explore the influence of the viewing angle and in order to develop tools for correcting the viewing angle artifact systematically, we carried out a preliminary study that compares analytical results with experimental data [28]. Our data indicated that the artifact becomes noticeable as the viewing angle exceeds 45°, which is in agreement with the previous studies [20-24].

3D imaging solutions are becoming increasingly popular in science, engineering and in everyday life; some of the progress being driven by the growing market for interactive gaming applications. During the past decade low cost 3D imaging solutions have reached the market. 3D imaging sensors can be classified into active and passive sensors. An active sensor first projects electromagnetic radiation onto the object, and the transmitted or reflected signal from the object is recorded. Laser triangulation, structured light, time of flight, holographic interferometry and holographic techniques fall into this class of methods [29]. A passive sensor records the

electromagnetic energy naturally emanating from the object, such as in stereo vision and photogrammetry [29]. In indoor 3D mapping applications, such as robotics and surveillance, low-cost sensors are more popular than expensive laser scanners [30]. One of the most popular, consumer-grade sensors developed in recent years is the Microsoft Kinect imager. It was originally designed for gaming applications, however, in recent years this sensor has revolutionized and driven research in 3D mapping in the indoor environment. Related applications are reviewed in the study of Henry et al. [31].

Incorporating temperature data captured by a 2D IR camera into the 3D depth map generated by a 3D imager, adds a new layer of complexity to the original 3D imaging problem. There are three major classes of systems used to generate 3D IR images. The first class comprises two IR cameras, which acquire two thermographic images of the same object [32, 33]. Based on point-pairs registration between the images acquired by the two IR cameras, the 3D surface of object can be inferred using the stereo vision method. The second class of systems consists of two digital cameras and one IR camera [12]. The 3D surface of the object is measured by the binocular subsystem of the digital camera pair, and the IR camera acquires 2D thermographic images of the object. 3D thermal map is then achieved by mapping the 2D temperature texture onto the 3D surface. The 3D surface maps computed by these two methods are based on stereo vision algorithms, which rely on the clear detection of feature points in color or IR images. Therefore, the accuracy of the 3D data depends on the texture of surface: for an object with well-defined feature points it performs with better accuracy. Often the natural feature points on the human body are not sufficient for an accurate 3D reconstruction, and artificial feature points have to be applied to improve measurement accuracy of the 3D structure.

The third class of systems that uses the structured light scanning technique to obtain accurate 3D surface data [34-36] is not dependent on the surface texture. Such a system usually includes a source that projects structured light (a grid pattern) onto the surface and one or more cameras that record the pattern formed on the surface. The 3D shape of the surface is computed from the deformation of the regular grid pattern. When compared with stereo vision systems, the system based on structured light has higher data acquisition rates and it is less computationally expensive [29].

The Microsoft Kinect is a low-cost and convenient option to implement structured light 3D imaging. It projects structured IR light onto the surface, and neither this light nor the projected pattern are detectable by the human eye. Therefore this form of imaging is comfortable to the patient in medical applications [37]. Another advantage is that Microsoft Kinect can generate depth maps at a relatively high frame rate of 30 fps with a resolution of 640×480 [30]. These features enable the device to capture the patient's motion in real-time [38]. Therefore the Kinect-based system developed for the present study holds the potential to enable dynamic 3D IR thermal map (measure 3D temperature evolution as a function of time) [39] with real-time motion tracking.

Over the past few years the Kinect imager has also become popular in a variety of scientific and technical imaging applications. Volumetric measurements achieved by the Microsoft Kinect are gaining attention in the medical community for breast cancer treatment evaluation [40] and lymphedema detection [41]. Thus, in addition to correcting for the viewing angle artifacts in 3D IR thermal map, implementations by Kinect can provide volumetric information to supplement the thermal signal, which can lead to more comprehensive data collection for medical diagnostic purposes.

To solve the measurement challenge caused by directional emissivity artifacts, researchers integrated 3D spatial information with IR thermal map to improve measurement accuracy. This combination of imaging techniques was used in engineering applications, such as in a wind tunnel experiment [42], for reconstruction of water waves [32], and for tracking and recognition of moving objects [43]. However, only a few researchers have tackled this issue in medical applications. Aksenov et al. [11] used thermal stereoscopy to characterize inflammation. Ju et al. [12] developed 3D thermographic imaging techniques to rectify the viewing angle artifact based on a heat flux model for the diagnosis of inflammation. They standardized face thermal mapping by a 3D facial shape template. The shortfall of this approach is that the heat flux model is not based on the fundamental behavior of the directional emissivity, and the angular variation was simplified by using the cosine function, which can lead to significant error. Very few studies have been reported that used the directional emissivity of skin to correct for the viewing angle artifact in in-vivo IR thermography using the 3D imaging technique [12] [11]. The objective of this paper is to introduce a versatile 3D IR imaging system relying on the inexpensive and popular Microsoft Kinect sensor that allows transient 3D temperature measurements of the human body suitable for quantitative medical diagnostic applications.

2. Methods

2.1 Imaging system and data acquisition

In this study, we introduce the 3D infrared imaging system shown in Figure 1. It consists of the Kinect for Windows® (Microsoft Corporation) 3D imager (top), and the infrared camera- Med Cam® (Hurley IR, Mt Airy, MD) (bottom), which contains the IR detector- THERMAL-EYE SERIES 17-640® (L-3 Communications Corporation, Dallas, TX).

The Kinect device has a field of view (FOV) of $57^{o} \times 43^{o}$ (Horizontal $\times$ Vertical), and acquires a RGB and depth image streams with a frame rate of 30 fps. The resolution of the RGB image is 1280×960, and the resolution of the depth image is 640×480. To reconstruct the 3D surface data for the human body, we used the Kinect device along with open-source software – ReconstructMe[44]. ReconstructMe can achieve real-time 3D reconstruction by scanning the human body from multiple directions, and the reconstructed 3D surface grid is stored in the format of polygon (.ply).

Figure 1 The 3D infrared imaging system combining the Kinect imager (top) and the infrared camera (bottom).

The infrared camera detects electromagnetic radiation in infrared spectrum of 7.5-13.5 μm with FOV of $57^{o} \times 43^{o}$ (Horizontal × Vertical). The camera is equipped with an uncooled amorphous silicon microbolometer focal plane array (FPA) having dimensions of 640×480. It acquires 16-bit raw data with resolution of 632×476 at a frame rate of 30 fps, and the IR camera has temperature sensitivity of 0.0315 ^{o} K. It is controlled by a PC using PCI Express Card - PIXCI® EB1, and IR images are acquired using a LabVIEW®-based software (version: 11.0.1, National Instruments Corporation, Austin, TX).

The 2D thermal image of the human body is acquired by the IR camera. Prior to image acquisition, we conducted black-body calibration to obtain the conversion between radiance detected by IR camera and the corresponding temperature. The radiance-temperature relationship is modeled by a fourth order polynomial as shown in Eq.(1). Within the range of temperatures used in the calibration, the infrared camera can generate the 2D thermal maps presented as temperature data, $T(°C)$, based on the polynomial of pixel intensity g:

$$T(°C) = -3.459387 \times 10^5 + 56.540702g - 0.003469g^2$$
$$+9.470542 \times 10^{-8}g^3 - 9.699380 \times 10^{-13}g^4 \quad . \tag{1}$$

In the wavelength range of 2 - 14 μm, the emissivity of human skin is in the range of 0.98 ± 0.01[45-47]. Therefore, the relative temperature measurements obtained using the parameters from the black-body calibration can easily be corrected for absolute values, as needed. On the other hand, the temperature difference between two measurement samples (two locations from the same image or data from different images recorded by the same camera) will be accurate without the need for correction. In quantitative diagnostic applications, temperature differences (local temperature increase for cancer [1-8, 48] or inflammation [49], and temperature decrease for ischemia [49], for example) between healthy and diseased regions of

the body are of particular interest. To validate the thermal mapping measured by IR camera, we also measured the temperature at selected locations on the skin with thermocouples. The thermocouple measurement was conducted using a USB-based data acquisition card (NI USB-9211®, National Instruments Corporation, Austin, TX).

2.2 The workflow of 3D IR imaging

Using the imaging system described in Section 2.1, the work flow leading to 3D thermal mapping with temperature correction can be summarized in four major steps: (1) system calibration, (2) 3D to 2D information mapping, (3) 2D to 3D information mapping and (4) curvature-induced artifact correction. The flowchart showing these four steps, along with their detailed algorithms is illustrated in Figure 2.

The objective of Step (1) - system calibration - is to determine the imaging system parameters to achieve the 3D-2D coordinate transformation between Kinect and the IR camera. This step is necessary, since the 2D (IR image) to 3D (Kinect coordinates) transformation is not unique. Therefore the 3D Kinect data are mapped into the 2D IR image first, in an intermediate step, followed by the stretching or the 2D thermal map into the 3D Kinect surface to generate the 3D raw thermal map. The camera parameters from Step (1) enable the 3D-2D information mapping in Step (2), in which the 3D spatial data acquired by Kinect are related to temperature in the 2D IR image. In Step (3) the combined Kinect-IR 2D data are stretched backed onto the 3D Kinect surface, by mapping pixel-by-pixel the IR temperature data onto the corresponding Kinect pixel data to generate the raw 3D thermal map. The empirical formula developed in this study (described in Section 2.6.5) is applied to the raw 3D thermal map in Step (4), the curvature-induced artifacts correction, to compensate for the temperature errors (apparent temperature decrease) due to the directional emissivity of skin. The details of each step are explained in the following sections.
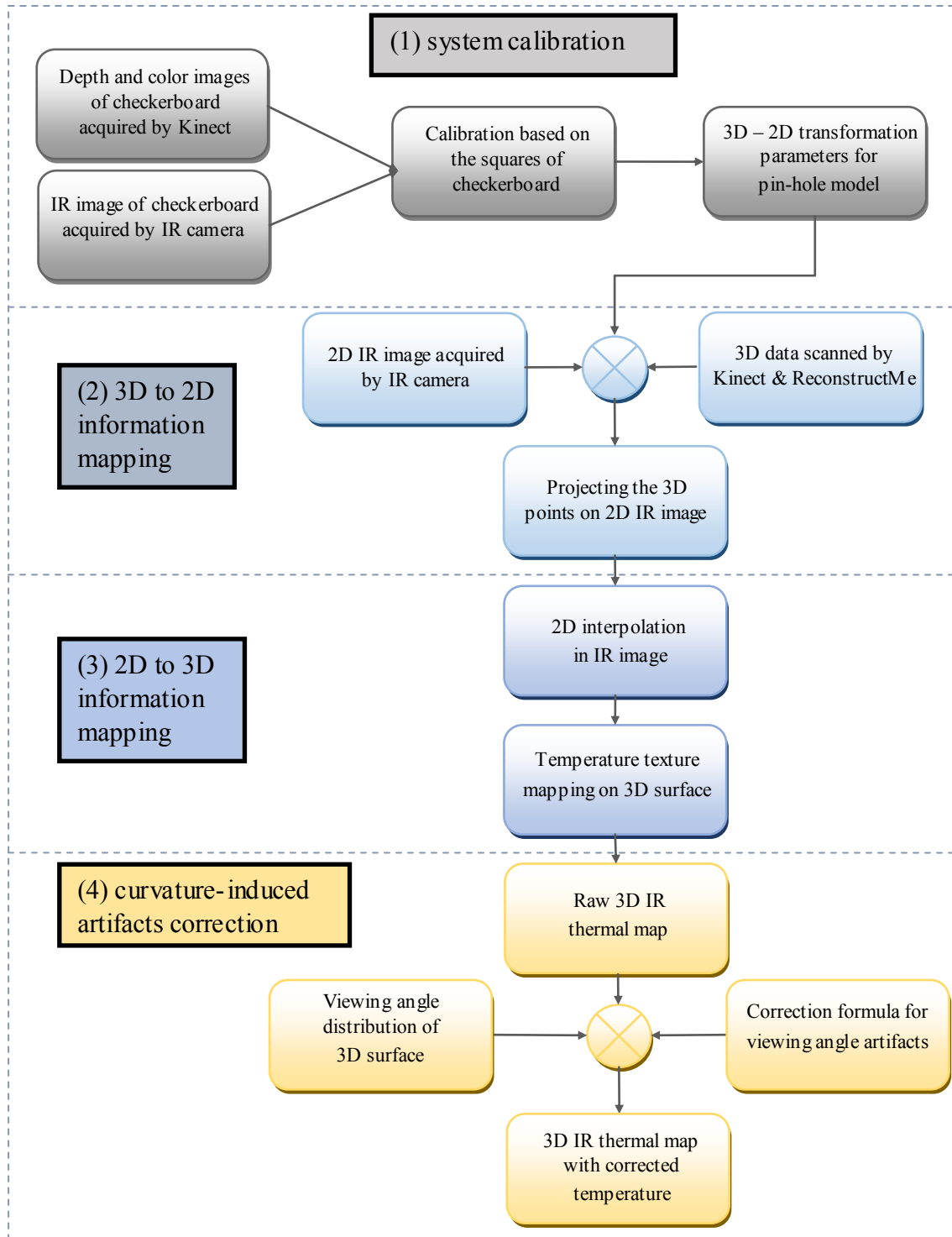
Figure 2 Flowchart of 3D thermal mapping with curvature correction, which includes four major steps: (1) system calibration, (2) 3D to 2D information mapping, (3) 2D to 3D information mapping, (4) curvature-induced artifacts correction.

2.3 System calibration

Mapping the thermal texture to 3D surface data relies on an accurate coordinate transformation between Kinect and IR cameras. The necessary transformation parameters are obtained via system calibration. In this study, we adopted the method and the MATLAB toolbox developed by Herrera et al. [50, 51] to determine the system parameters.

The calibration toolbox is based on the pinhole camera model developed by Heikkila[52], which consists of a perspective projection model and a correction model for lens distortion. We also utilized the MATLAB toolbox developed by Herrera et al. [50, 51]. The toolbox provides an established platform capable of simultaneously calibrating the external and internal parameters of the three cameras: the color camera and depth cameras of Kinect (the two Kinect cameras are mounted into the same housing, Fig. 1, top), and the IR camera (Fig. 1, bottom). The instrumentation steps, including image acquisition, calibration computation, and image processing, are all implemented using MATLAB 2013 (MathWorks Inc., Natick, MA).
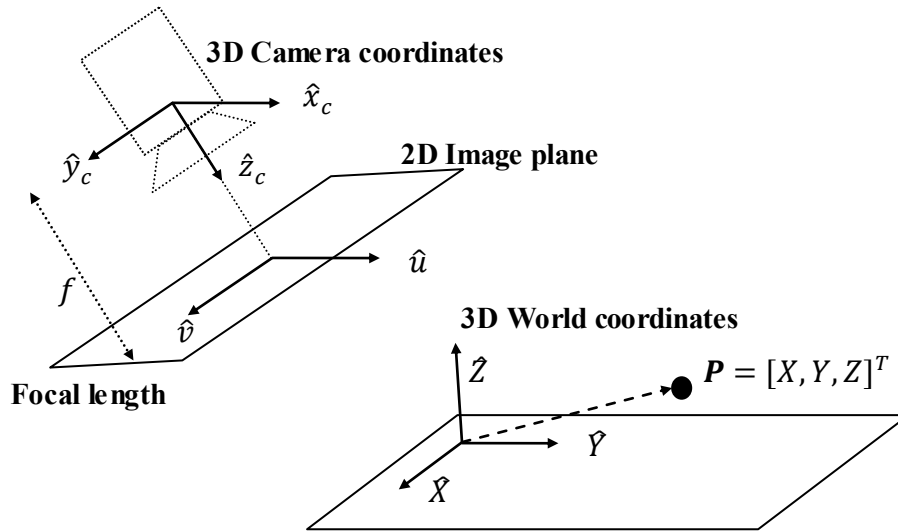

Figure 3 Schematic of the pinhole camera model used in imaging system calibration

2.3.1 Camera model for system calibration

By adopting a notation similar to that used in the literature [36, 42, 50], the schematic of the pinhole camera model [52] is illustrated in Figure 3. This schematic illustrates the linear transformation between the 3D world coordinates and the 2D image plane.

Given a point $\boldsymbol{P} = [X, Y, Z]^T$ in 3D world coordinates, and letting $\boldsymbol{p} = [u, v]^T$ be the corresponding coordinates in the 2D image plane, the linear transformation between these two points can be formulated as

$$\begin{bmatrix} u \\ v \\ 1 \end{bmatrix} \propto \boldsymbol{KT} \begin{bmatrix} X \\ Y \\ Z \\ 1 \end{bmatrix} \quad . \tag{2}$$

In Eq. (2) T denotes the transformation between the 3D world coordinates and the 3D camera coordinates. T contains the external parameters, the rotation matrix R and the translation vector t, described as

$$T = \begin{bmatrix} R & t \\ 0 & 1 \end{bmatrix} .$$ (3)

The term K in Eq. (2) is the matrix containing the internal parameters of camera, and it describes the projection from 3D camera coordinates to the 2D image plane as

$$K = \begin{bmatrix} \alpha f & 0 & u_{0c} & 0 \\ 0 & f & v_{0c} & 0 \\ 0 & 0 & 1 & 0 \end{bmatrix} .$$ (4)

In Eq. (4) α is the pixel aspect ratio of the image plane, f is the focal length of the camera, i.e. the distance between the projection center and the image plane. $[u_{0c}, v_{0c}]^T$ is the principal point, which is defined as the pixel coordinate for the center of image plane.

Using the linear projection described by Eqs. (2)-(4), given a point $P = [X, Y, Z]^T$ in 3D world coordinates, we can first compute the corresponding coordinate $p_c = [x_c, y_c, z_c]^T$ in 3D camera coordinates. According to the model of perspective projection in homogenous coordinates [53], by dividing the first two components of p_c, $[x_c, y_c]^T$, with its third component z_c, we obtain the linear projection $[x_u, y_u]^T$ on the 2D image plane of the camera as

$$\begin{bmatrix} x_u \\ y_u \end{bmatrix} = \frac{1}{z_c} \begin{bmatrix} x_c \\ y_c \end{bmatrix} .$$ (5)

In Eq. (5) $[x_u, y_u]^T$ is the ideal projection of p_c without considering the non-linear effects arising in practice. The pinhole model developed by Heikkila [52] also accounts for the radial and tangential distortion introduced by the lens. Using the undistorted projection $[x_u, y_u]^T$, the distorted projection $[x_d, y_d]^T$ on the image plane is modeled as

$$\begin{bmatrix} x_d \\ y_d \end{bmatrix} = (1 + k_1 r^2 + k_2 r^4 + + k_5 r^6) \begin{bmatrix} x_u \\ y_u \end{bmatrix} + d_x$$ (6)

$$d_x = \begin{bmatrix} 2k_3 x_u y_u + k_4 (r^2 + 2x_u^2) \\ k_3 (r^2 + 2y_u^2) + 2k_4 x_u y_u \end{bmatrix} .$$ (7)

In Eqs. (6) and (7) the terms $r^2 = x_u^2 + y_u^2$ and $[k_1, k_2, k_3, k_4, k_5]$ represent the distortion coefficients of the camera. Consequently, the distorted pixel location $[u_d, v_d]^T$ in the acquired 2D image is computed based on $[x_d, y_d]^T$ as

$$\begin{bmatrix} u_d \\ v_d \end{bmatrix} = \begin{bmatrix} \alpha f & 0 \\ 0 & f \end{bmatrix} \begin{bmatrix} x_d \\ y_d \end{bmatrix} + \begin{bmatrix} u_{0c} \\ v_{0c} \end{bmatrix}. \tag{8}$$

In Eq. (8) α is the pixel aspect ratio in the 2D image, f is the focal length of the camera, and $[u_{0c}, v_{0c}]^T$ is the principal point of 2D image plane, as described in Eq. (4).

2.3.2 Imaging setup for system calibration

To determine the external and internal parameters of the system, the imaging setup for system calibration is illustrated in Figure 4. The coordinate systems of the three cameras, the color and depth cameras of Kinect, and of the IR camera are denoted by {C}, {D}, and {I}, respectively. A planar checkerboard with 8×8 squares, shown in Fig. 5(a), is used to generate the 3D world coordinates for the pinhole model. For calibration purposes, the images of the planar checkerboard are simultaneously acquired by the three cameras. In order to mark the locations of the square corners detectable in the IR image, we inserted metal drawing pins at each corner of checkerboard squares, as shown in Fig. 5(b). The emissivity difference between the metal pins and the surface of the checkerboard creates a contrast in the IR image. The contrast enables us to identify the location of these corners in the IR image. During the image acquisition, we also tried to enhance the contrast of the metal pins and background by reflecting the thermal radiation from surrounding heat sources (such as human body and lighting) on an ad hoc basis.
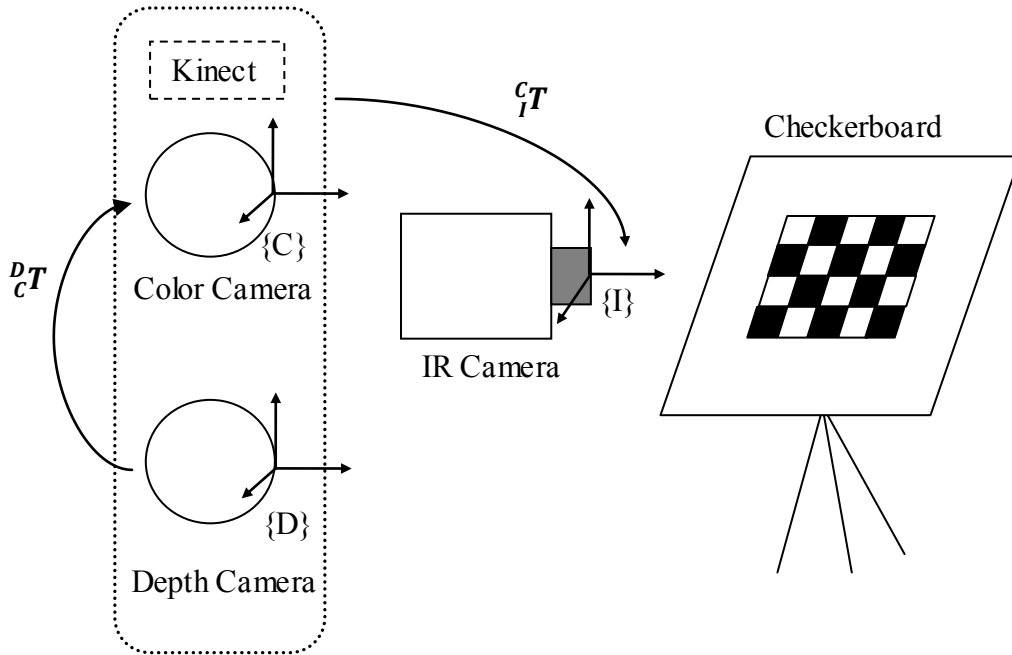

Figure 4 Schematic of the imaging setup for system calibration with 3D camera coordinates used in calibration: color camera {C} and depth camera {D} of Kinect, and the IR camera {I}.
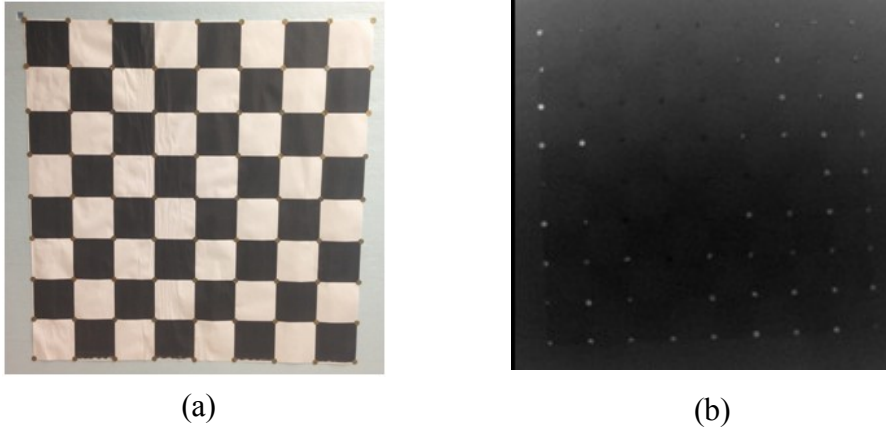
(a)   (b)

Figure 5 (a) Checkerboard for camera calibration and (b) the IR image of the checkerboard with metal pins located at the corners of each square.

According to the calibration methodology developed by Herrera et al. [50, 51], we acquired three sets of checkerboard images with the three cameras: a color image, a depth image, and an IR image. In addition, the checkerboard was positioned with three orientations for each camera, as illustrated in Fig. 6. At each orientation, the distance between the checkerboard and the cameras was also varied, and images with the three cameras were acquired simultaneously at each combination of orientation/distance. Images were acquired at 8 distances with three orientations, thereby leading to 24 images per camera. In the acquired image datasets, we manually selected the locations of the checkerboard corners in both color and IR image datasets (the corner locations in the IR image are pinpointed by the metal pins), and the locations of checkerboard edges were selected in the depth image datasets. Via the relation of location correspondence provided by these control points, the camera parameters were iteratively optimized using the Levenberg-Marquardt algorithm, as described in [50].
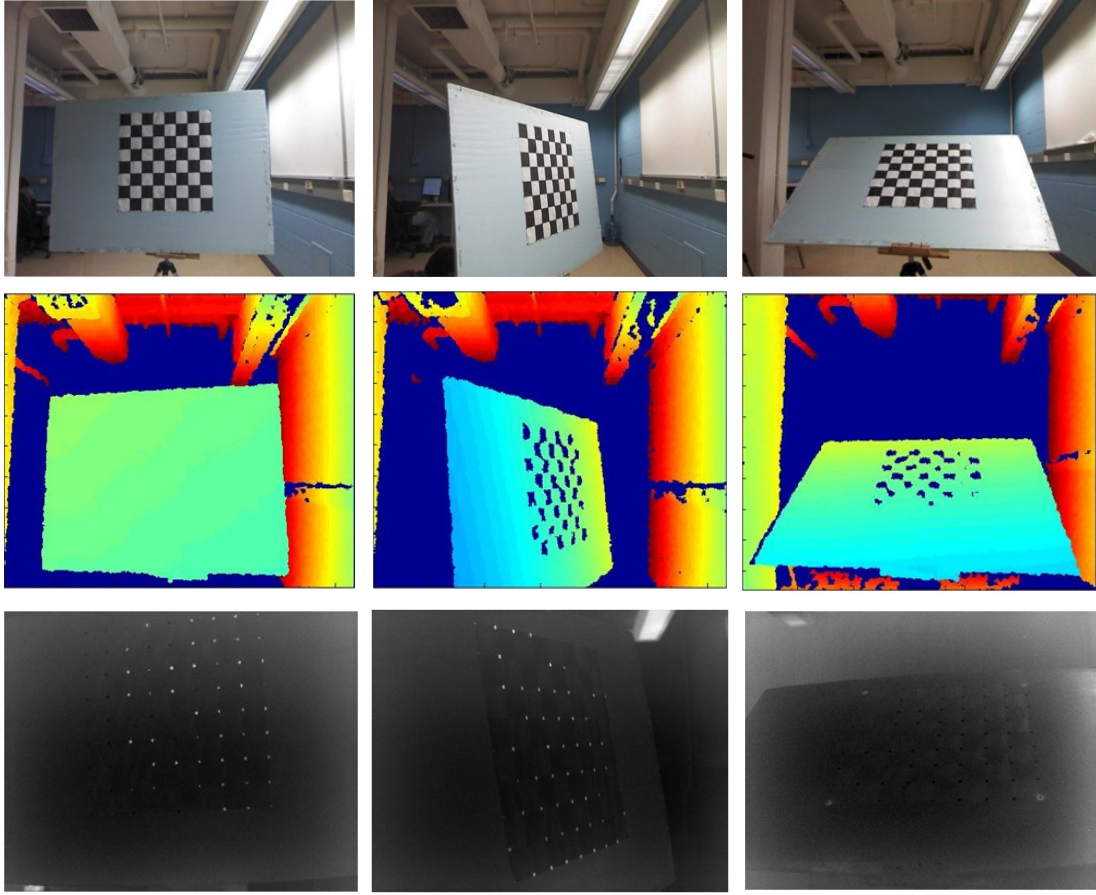
Figure 6 In system calibration, three image sets of the checkerboard with three orientations were acquired: color images acquired by Kinect (top row), depth images acquired by Kinect (middle row), and IR images acquired by the infrared camera (bottom row).

2.4 3D - 2D information mapping

The next step in obtaining the 3D thermal map is the mapping of the depth information into 2D, to associate depth data to the corresponding temperature in the IR image. The camera parameters obtained from system calibration enable an accurate coordinate transformation from the Kinect device to the IR camera. In our application, the transformation from the depth camera to the IR camera is of particular interest, so that the 3D spatial information can be associated with the 2D thermal mapping in the IR image. We can achieve the transformation using the matrices: ${}^{D}_{C}T$ and ${}^{C}_{I}T$ as indicated in Fig. 4, in which ${}^{D}_{C}T$ represents the transformation between the depth camera and the color camera, and ${}^{C}_{I}T$ represents the transformation between the color camera and the IR camera. These two matrices are obtained in the procedure of system calibration. According to Eq.(3), the 3D coordinate x_d in the depth camera frame {D} can be transformed to the coordinate x_c in the color camera frame {C} using the matrix

$$ {}^{D}_{C}T = \left\{ {}^{D}_{C}R, {}^{D}_{C}t \right\} , \qquad (9) $$

where $^D_C R$ and $^D_C t$ represent the rotation matrix and the translation vector in $^D_C T$. The color camera coordinate x_c is determined as

$$x_c = {}^D_C R x_d + {}^D_C t .$$ (10)

Next, via x_d and the transformation between the IR camera and color camera

$$^C_I T = \{ {}^C_I R, {}^C_I t \} ,$$ (11)

the corresponding point x_i in the IR camera frame {I} can be computed as

$$x_i = {}^C_I R x_c + {}^C_I t .$$ (12)

In this way, any 3D point located in the Kinect depth camera frame can be projected to the corresponding 2D coordinates in the IR image to allow the association of depth and temperature information. Since the reference coordinates of ReconstructMe correspond to those of the depth camera of Kinect, any 3D point x_d scanned by ReconstructMe can be transformed from the depth camera to the corresponding point x_i in the IR camera by consecutively applying Eqs. (9)-(12).

After the 3D data are transformed from the depth camera to the IR camera, the corresponding 2D pixel coordinate in the IR image can be computed based on the internal parameters of the IR camera and Eqs. (5)-(8). This step completes the 3D-2D mapping using the parameters obtained from the system calibration.

2.5 2D - 3D information mapping

The next step in the generation of the 3D thermal map is the stretching of the 2D information onto the 3D depth map to generate the raw 3D thermal map. In this step the 2D IR image is overlaid with the point projected from the 3D data. Since there are more data points on the 3D surface than in the 2D infrared image, linear 2D interpolation is used to generate the missing temperature data. The raw thermal map on the 3D surface was generated based on the 2D temperature texture acquired in the IR image.

2.6 Curvature-induced artifact correction

As addressed in the introduction section, because of the artifact associated with directional emissivity, for any point on the curved surface, the temperature recorded by the IR detector may appears lower than the actual temperature of the surface. In this section, we first introduce the models for the directional emissivity and the experimental data that was acquired in our pervious study [28], which demonstrates the influence of surface curvature on temperature measurment. Based on the experimental data, a three-step correction algorithm is derived to compensate for the artifacts caused by the directional emissivity in the implementation of 3D thermal mapping, as presented in Step (4) in Fig.2.

2.6.1 The dielectric and non-dielectric models of directional emissivity

In the literature, there are two classical models that have been used to describe the directional emissivity of skin in the infrared spectrum, the dielectric [45] and the non-dielectric [54] models.

These two models are based on different assumptions for the electromagnetic properties of skin. They provide an analytical basis to estimate skin emissivity as a function of the viewing angle, $\varepsilon(\theta)$, where the viewing angle θ is defined as the angle between the surface normal and the axis of the IR camera.

Using the index of refraction n_s of a material, Watmough et al. [45] derived the expression for the directional emissivity $\varepsilon(\theta)$ as a function of viewing angle θ as

$$\varepsilon(\theta) = 1\text{-}0.5\left(\frac{\beta-\cos\theta}{\beta+\cos\theta}\right)^2 \cdot \left[1 + \left(\frac{\beta\cos\theta-\sin^2\theta}{\beta\cos\theta+\sin^2\theta}\right)^2\right] , \tag{13}$$

with

$$\beta = \sqrt{n_s{}^2 - \sin^2\theta} \quad . \tag{14}$$

Based on this model, the skin can be modeled as a dielectric material having a real component of index of refraction greater than unity with respect to air.

The non-dielectric model of directional emissivity was developed by Hejazi and Spangler [54]. In this model, skin is treated as a lossy dielectric material, and instead of the real index of refraction used for a dielectric material, the index of refraction for a non-dielectric material is modeled as a complex function

$$\boldsymbol{n_s} = n_s + jk_s, \quad \boldsymbol{n_a} = n_a , \tag{15}$$

where n_s and n_a represent the index of refraction for skin and air, respectively. In Eq.(15) n_s and n_a are the real parts, and k_s is the attenuation coefficient. According to the derivation reported by Siegel and Howell [55], the directional emissivity $\varepsilon(\theta)$, which is a function of viewing angle θ, is related to the refraction indices, n_s and n_a, and the attenuation, k_s, as

$$\varepsilon(\theta) = 1 - \rho(\theta) \tag{16}$$

where

$$\rho(\theta) = \frac{\rho_\parallel(\theta)+\rho_\perp(\theta)}{2} \quad . \tag{17}$$

As shown by Hajazi and Spangler [54], the numerator in Eq.(17) can be expressed as

$$\rho_\perp(\theta) = \frac{(q-n_a\cos(\theta))^2+p^2}{(q+n_a\cos(\theta))^2+p^2} \qquad \text{and} \tag{18}$$

$$\rho_\parallel(\theta) = \frac{[(n_s^2-k_s^2)\cos\theta-n_a q]^2+[2n_s k_s\cos\theta-n_a p]^2}{[(n_s^2-k_s^2)\cos\theta+n_a q]^2+[2n_s k_s\cos\theta+n_a p]^2} , \tag{19}$$

where

$$p^2 = \tfrac{1}{2}[-n_s^2 + k_s^2 + n_a^2\sin^2\theta] + \tfrac{1}{2}\sqrt{4n_s^2 k_s^2 + (n_s^2 - k_s^2 - n_a^2\sin^2\theta)^2} \tag{20}$$

$$q^2 = \tfrac{1}{2}[n_s^2 - k_s^2 - n_a^2\sin^2\theta] + \tfrac{1}{2}\sqrt{4n_s^2 k_s^2 + (n_s^2 - k_s^2 - n_a^2\sin^2\theta)^2} \tag{21}$$

2.6.2 Modeling of the directional emissivity of skin

When the skin surface is normal to the camera axis with a viewing angle $\theta = 0°$, the skin emissivity ε_0 is in the range of 0.98 ± 0.01 in the infrared spectrum range of 2-14 µm [45-47]. By adopting this as the nominal value of emissivity ε_0 along with the optical properties of skin from Ref. [54], we can model the directional emissivity of the skin using the two models introduced in Sec.2.6.1. In addition, we modeled the directional emissivity $\varepsilon(\theta)$ using the cosine function as $\varepsilon(\theta) = \varepsilon_0 \cos \theta$ for reference. This simplified expression is commonly used to describe the directional emissivity of an object when adequate, more accurate models are unavailable. The parameters used for these three models are summarized in Table 1, and the resulting directional emissivity plots are contrasted in Fig.7.

Table 1 Parameters used for modeling the directional emissivity of skin

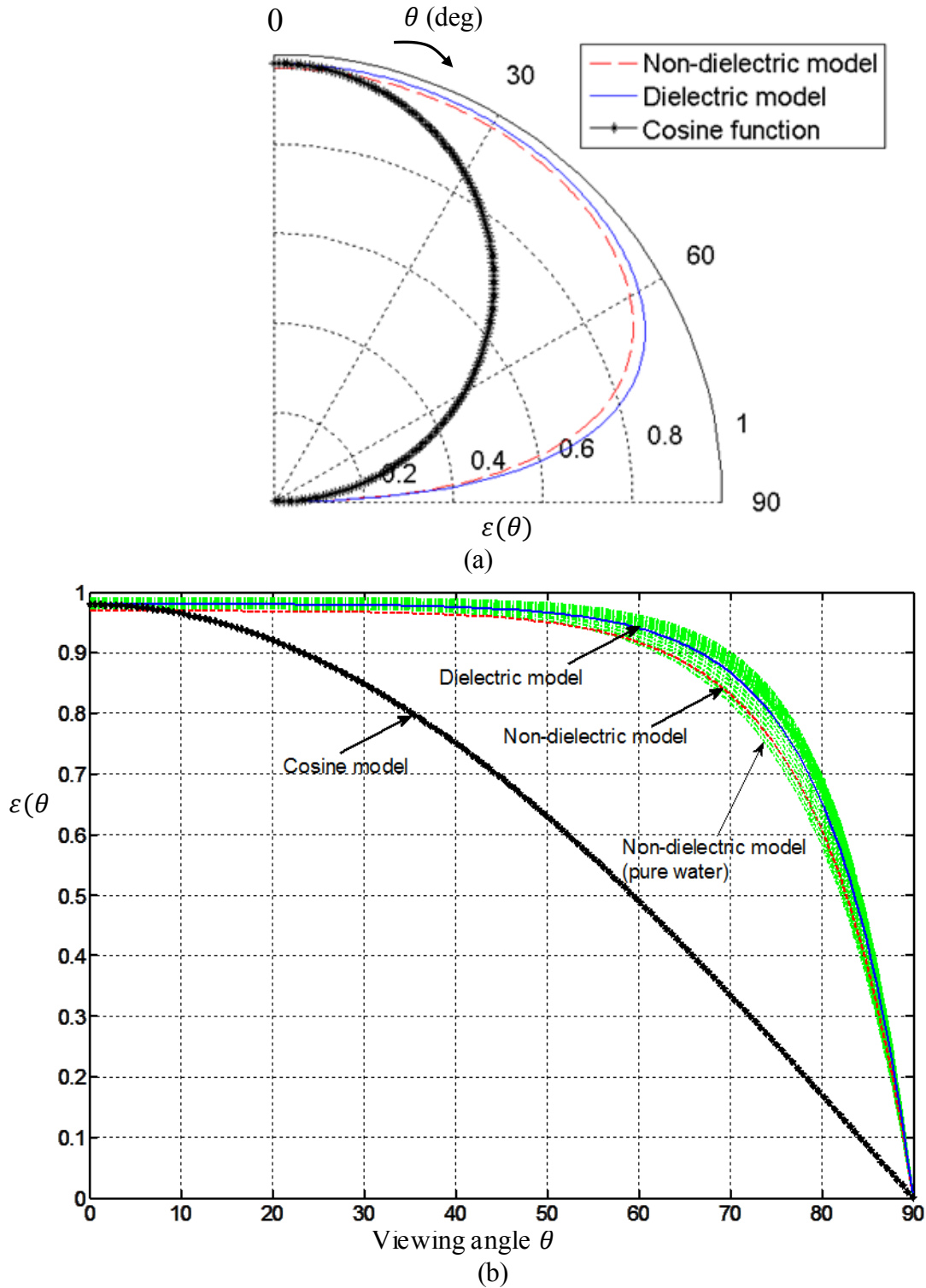|	
Dielectric model [45]	$n_s = 1.33$
Non-dielectric model [54]	$n_s = 1.33, \ k_s = 0.25, \ n_a = 1$
Cosine model[45-47]	$\varepsilon_0 = 0.98$

Figure 7 Directional emissivity of the skin $\varepsilon(\theta)$ plotted as a function of the viewing angle using the dielectric model [45], the non-dielectric model [54], and the cosine function: (a) Polar plot and (b) Cartesian plot with directional emissivity of pure water at 310 K (green curves), which is computed by the non-dielectric model using appropriate wavelength-dependent refractive index values for the infrared spectral range: 7.5-13.5 μm.

2.6.3 Model validation for the directional emissivity of skin

Considering the fact that the optical properties of skin in the infrared spectrum are dominated by pure water, we used the wavelength-dependent refractive index of pure water at 310 K (body temperature) to validate directional emissivity values of skin computed by the dielectric and non-dielectric models in the previous section. We acquired refractive index $[n_\lambda, k_\lambda]$ data in the wavelength range, $\lambda=7.5\text{-}13.5$ µm, which match the spectral ranges detected by the IR camera used in this study (see Section 2.1 for details). The refractive index at each wavelength is obtained using the classical oscillator model developed by The Johns Hopkins University Applied Physics Laboratory (APL) [56, 57] and the optical properties of pure water in Ref. [58] . The values of the refractive index $[n_\lambda, k_\lambda]$ at each wavelength λ were then taken as $[n_s, k_s]$ in the non-dielectric model [54]. Multiple plots of the directional emissivity function, for pure water $\varepsilon_\lambda(\theta)$ were generated, one for each wavelength within the wavelength range of interest, as presented by the green curves in Fig. 7(b). The directional emissivities of skin computed by the dielectric and non-dielectric models are also plotted in Fig.7(b) for comparison. Fig. 7(b) demonstrates that the directional emissivity of skin computed by both dielectric and non-dielectric models agrees well with that of pure water in these two spectral ranges. The validation suggests that under conditions (temperature and wavelength) characteristic of our applications, both dielectric and non-dielectric models can provide reasonable approximation for the directional emissivity of the skin.

2.6.4 IR Imaging experiments for the phantom with curved surface

To quantify the relation between the detected temperature in IR image and the directional emissivity, an empirical model was proposed in our preliminary study [28]. In the study[28] the surface temperature of a cylindrical phantom with anodized aluminum surface was measured using IR imaging as shown in Fig. 8(a) (more details about the experimental conditions are available in [28]). To analyze the temperature variation caused by viewing angle, 0-90º, we sampled the surface area marked by four lines in Fig.8(a); the two lines on the left and right hand sides indicate the range for which viewing angle is considered. The top and bottom lines encompass the horizontal region for averaging.

As proposed by Clark [19], if we take the temperature difference between the curved surface and the environment into account, at the shorter wavelengths, the measurement error of object temperature due to its directional emissivity can be estimated by the linearized relation for small temperature intervals [19] as

$$\Delta T^c \equiv \frac{T_s - T(\theta)}{T_s - T_a} = \frac{\Delta T}{T_s - T_a} = C(1 - \varepsilon(\theta)),\tag{22}$$

where ΔT^c is the dimensionless form (in the range 0-1) of the temperature decrease detected in IR image. In Eq. (22) ΔT is the temperature difference between the actual temperature of the surface T_s and the measured temperature at the viewing angle θ, $T(\theta)$. ΔT^c is calculated by normalizing ΔT with respect to the difference between the actual temperature, T_s and the ambient temperature of the imaging environment T_a. On the right hand side of Eq. (22), $\varepsilon(\theta)$ is the directional emissivity at viewing angle θ, and C is the constant representing the linear relation between ΔT^c and $(1 - \varepsilon(\theta))$.

To validate the relation proposed by Clark [19], Eq.(22), we computed the mean value of $\Delta T^c = T_s - T(\theta)/T_s - T_a$ for the six temperatures considered (34ºC - 44ºC) in the study [28] and plot the results in Fig.8(b). In the same plot, the values $1 - \varepsilon(\theta)$ computed using the three models for directional emissivity $\varepsilon(\theta)$ (dielectric, non-dielectric, and cosine models), are also plotted in Fig.8(b) for comparison. According to the optical properties of anodized aluminum[59], we set n_s=2.84 in the dielectric model, which leads to the nominal emissivity ε_0 =0.77 [59] of anodized aluminum at normal orientation (θ= 0). In the non-dielectric model, the nominal emissivity of ε_0 =0.77 is used again, and the values n_s=2.84 and k_s =0.0003 were assumed based on the Ref. [60]. The refractive index of air n_a is set to 1.

The combined results in Fig.8(b) suggest that the mean value $of \Delta T^c$ (blue data points) matches very well the theoretical prediction for $1 - \varepsilon(\theta)$ computed using the dielectric and non-dielectric models. The plots obtained using the dielectric and non-dielectric models are nearly identical when the optical properties of anodized aluminum are used in the model. Therefore, the observed agreement between experimental ΔT^c and $1 - \varepsilon(\theta)$ predicted by dielectric and non-dielectric models supports the linear approximation proposed by Clark [19] (Eq. (22)). In contrast, such agreement cannot be observed between ΔT^c and the $1 - \varepsilon(\theta)$ that is predicted by the cosine model. For θ greater than 10 degrees the cosine substantially overestimates the decrease of emissivity caused by viewing angle, as shown in Fig.8(b),.
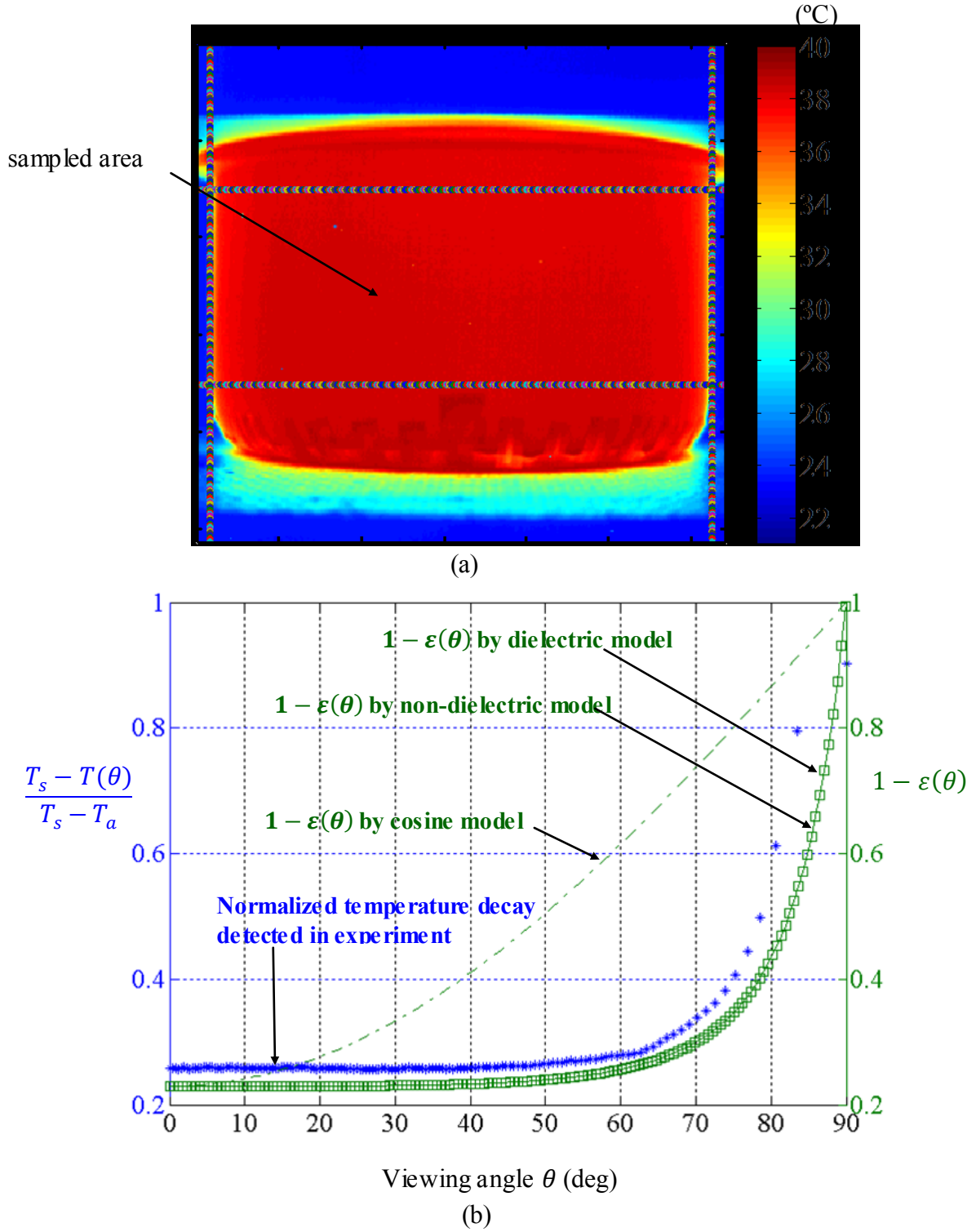
Figure 8 (a) Color-coded IR image of the cylindrical curved surface (water temperature = 44ºC) with marked margins indicating the region for analysis. (b) Mean value of the measurement error for the six temperatures (34ºC - 44ºC) (left axis) used in cylindrical phantom experiment [28] and the computed value of $1 - \varepsilon(\theta)$ (right axis) as function of the viewing angle.

2.6.5 Derivation of empirical formula for temperature correction

Based on the similarity between computational results (Eq.(22)) and experiment (Fig.8(b)), with the constant C assumed to be 1 in Eq.(22), the similarity relationship can be approximated as

$$\Delta T^c \equiv \frac{T_s - T(\theta)}{T_s - T_a} = \frac{\Delta T}{T_s - T_a} \sim 1 - \varepsilon(\theta) \; , \tag{23}$$

where $\Delta T = T_s - T(\theta)$ denotes the difference between the actual and detected temperatures at the viewing angle θ. Thus, using the approximation described by Eq. (23), we can further derive an empirical correlation to estimate the temperature measurement error, ΔT. By knowing the directional emissivity $\varepsilon(\theta)$, the temperature $T(\theta)$ detected in the IR image, and the difference between the actual temperature T_s and the ambient temperature T_a, ΔT can be estimated as

$$\Delta T \equiv T_s - T(\theta) \approx \left(1 - \varepsilon(\theta)\right)(T_s - T_a). \tag{24}$$

Therefore, given the directional emissivity $\varepsilon(\theta)$ that can be expressed analytically using the emissivity models [45] [54] presented in Section 2.6.1, without the loss of generality, we can continue the derivation by assuming the equivalence between the two sides of Eq.(24). The actual temperature, $T_s(\theta)$, can be expressed in terms of $T(\theta), T_a$, and $\varepsilon(\theta)$ as

$$T_s(\theta) - T(\theta) = \left(1 - \varepsilon(\theta)\right)(T_s(\theta) - T_a)$$

$$T_s(\theta) = \frac{T(\theta) - (1 - \varepsilon(\theta))T_a}{\varepsilon(\theta)} \; . \tag{25}$$

Eq.(25) is the first step of the correction algorithm, which recovers the actual temperature $T_s(\theta)$ from the value $T(\theta)$ measured by IR imaging.

Due to the imperfect emissivity models for $T_s(\theta)$, Eq.(25) may still contain the unknown bias in which the variation of surface curvature is not taken into account. Therefore, in the second step of the correction algorithm, the quantity $T_s(\theta)$ is calibrated with respect to an unbiased temperature measurement sampled from the region of the IR image where the curvature-induced artifact is absent. The unbiased temperature is sampled at the location with zero viewing angle $T_0 = T(\theta = 0)$ in the IR image to minimize the artifact induced by the viewing angle. The biased temperature prediction obtained using Eq.(25), $T_s^0 = T_s(\theta = 0)$, is also computed at the same location. By taking the ratio of T_s^0 and T_0, we find the scaling factor

$$S = \frac{T_0}{T_s^0} = \frac{T(\theta = 0)}{T_s(\theta = 0)} \tag{26}$$

that can be used to calibrate T_s^0 to determine the unbiased temperature observation T_0. We can then utilize S to calibrate the biased temperature value $T_s(\theta)$ (from Eq.(25)) at all locations (for a range of viewing angles θ) in the same IR image. The accurate temperature $T_s^*(\theta)$ after calibration and accounting for the curvature induced artifacts can be found as

$$T_s^*(\theta) = S \cdot T_s(\theta) \quad . \tag{27}$$

For validation purposes, we applied the correction procedures described by Eqs.(25)-(27) to the IR image acquired in the cylindrical phantom experiment (Section 2.6.4). The image on the left hand side of Fig.9 (a) is the color-coded IR image of the cylindrical phantom before applying the described correction algorithm. The surface of phantom is isothermal in the experiment, and the viewing angle θ increases symmetrically toward the perimeter of phantom.

According to Eq.(25), we first applied the non-dielectric model [54] to compute the directional emissivity of the cylindrical phantom using the optical properties described in Section 2.6.4. In the second step, the average temperature along the central vertical line on the phantom surface (the vertical black line in Fig.9(a)), where the viewing angle $\theta = 0$, was taken as the unbiased observation T_0 in Eq.(26) to determine the scaling factor S. Finally, the scaling factor S is used to multiply the predicted temperature $T_s(\theta)$ obtained using Eq.(25) at all other locations. The resulting phantom image after applying the three-step correction algorithm is shown on the right hand side of Fig.9(a). To quantify the temperature distribution before and after the correction, the 1D temperature profiles along the horizontal direction are plotted in Fig. 9(b) as a function of the viewing angle. As the viewing angle exceeds 40° we can clearly observe a temperature drop towards the sides of phantom surface prior to the correction. The temperature profile becomes more uniform after correction (right hand side plot of Fig.9(b)). We observe that in the range of 40° to 60°, the temperature decrease associated with the directional emissivity is uniformly rectified. Since the phantom surface is isothermal, the recovered uniformity of the temperature profile after correction validates the correction procedure described by Eqs.(25)-(27).
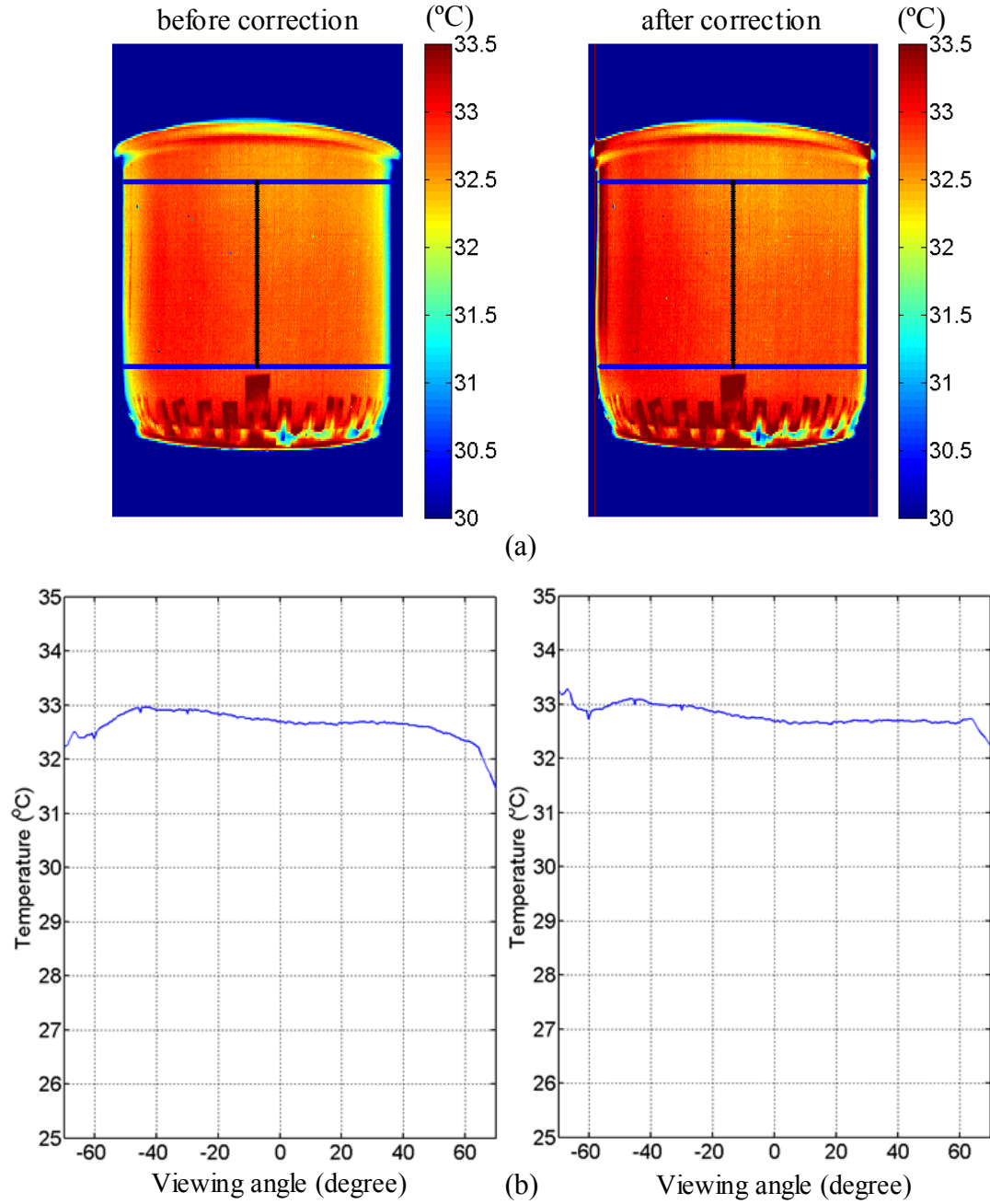
Figure 9 Results of applying the three-step correction algorithm (ambient temperature $T_a = 23$℃) to the IR images of the cylindrical phantom: (a) Color-coded IR images before (left) and after (right) correction. The mean temperature along the central vertical line (black line) is taken as the unbiased observation for calibration (Eq.(26)). Mean value of the temperature as a function of the viewing angle before (left) and after (right) correction (temperature is averaged vertically within the rectangular region bordered by two horizontal blue lines in (a)).

According to the theory introduced above, the raw 3D thermal map generated by the IR camera can be corrected using the three-step approach described by Eqs. (25)–(27). This is accomplished using the analytical expression for the directional emissivity $\varepsilon(\theta)$ of the object and the viewing angle distribution θ (x,y,z) on the surface.

After mapping the temperature texture from IR image to the 3D surface as described in Section 2.5, we apply the three expressions for the directional emissivity $\varepsilon(\theta)$ to the resulting 3D raw thermal map based on the three emissivity models introduced in Section 2.6.1, the dielectric [45], non-dielectric [54], and cosine models. To correct for the directional emissivity of the skin $\varepsilon(\theta)$, the viewing angle θ distribution on the 3D surface is first computed using the normal vector for each unit area as

$$\theta = cos^{-1} \left| \frac{\vec{Z} \cdot \vec{n}}{|\vec{Z}|} \right| \quad . \tag{28}$$

In Eq.(28) $\vec{Z}$ is the 3D vector of the axis of the IR camera, $[0,0,1]^T$ in our coordinate system, and $\vec{n}$ is the normal vector of a unit area of the surface being imaged.

3. Results

3.1 The workflow of image processing

Based on the procedures described in previous sections, Fig. 10 illustrates the flowchart of the image processing steps along with the corresponding image data generated in each step. In this section, the content of the image data processed at each step will be described in detail, and the correction results discussed. According to the flowchart in Fig.10, we first acquired the images of the human body using Kinect and the IR camera, as illustrated by the procedure following Step (1). The 3D-2D transformation parameters from Step (1) were applied to Step (2) to achieve the 3D to 2D mapping. By applying the 2D interpolation and 2D-3D mapping, the raw 3D IR thermal map was generated in Step (3). Finally, the curvature-induced artifacts were corrected for to generate the final accurate 3D thermal map in Step (4).

3.2 Three dimensional surface reconstruction and the validation of camera parameters

To illustrate Steps.(1)-(4) in Figure 10, the images acquired by the depth camera and IR camera are shown in Figure 11. The 3D surface was reconstructed using ReconstructMe (v1.1.74) [44] as shown in Fig. 11(a), and Fig. 11(b) shows the color coded 2D temperature distribution of the body surface acquired by the IR camera. Using the transformation parameters obtained from the system calibration, the coordinates of the 3D grid of surface (Fig. 11(a)) were transformed to the 2D image coordinates as shown in Fig. 11(c). Next, the 2D IR image is overlaid with the points projected from the 3D data, as shown in Fig.11(d). The alignment between the 2D projection and the underlying IR image is used to validate the parameters from system calibration.
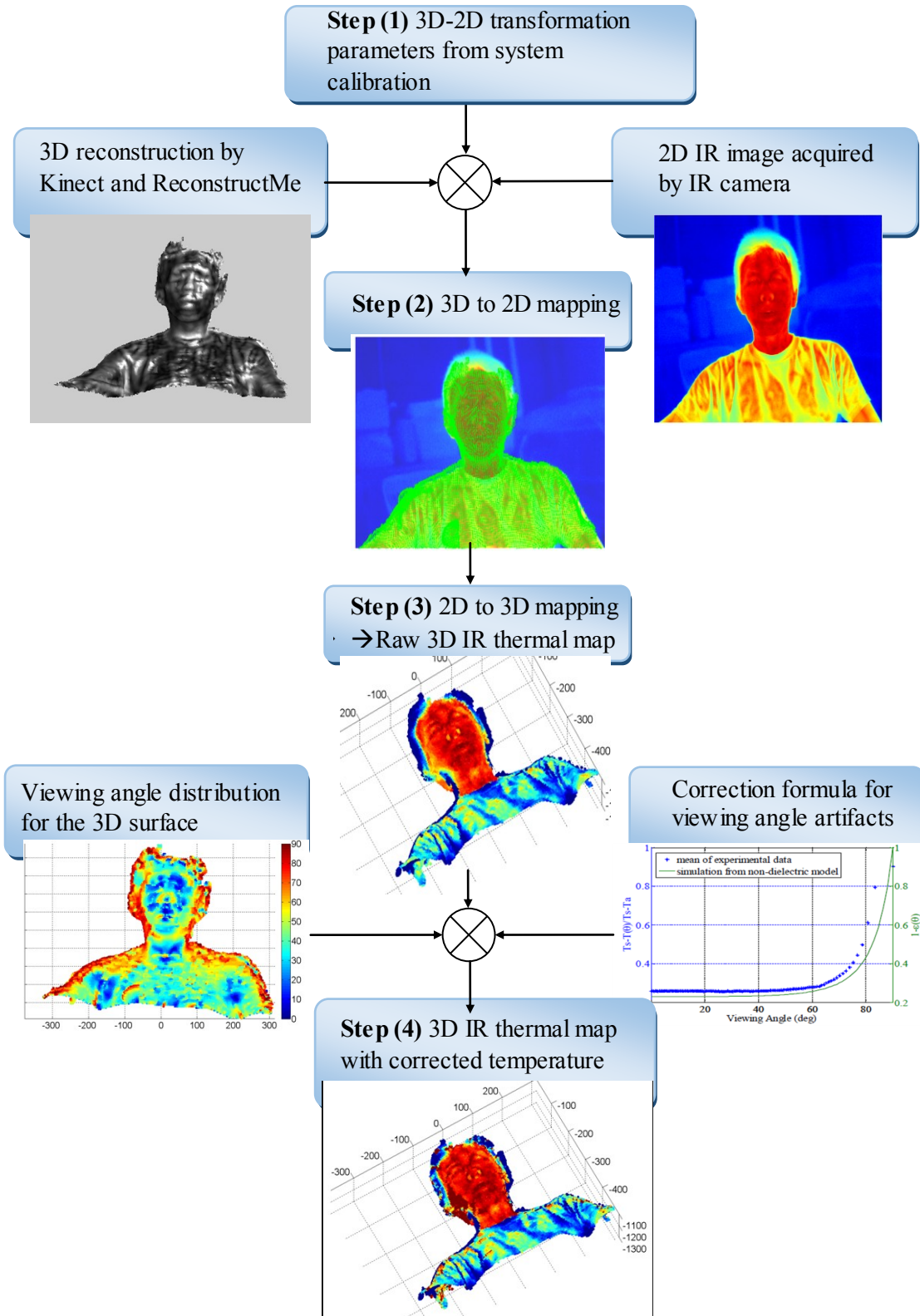
Step (1) 3D-2D transformation parameters from system calibration

3D reconstruction by Kinect and ReconstructMe

2D IR image acquired by IR camera

Step (2) 3D to 2D mapping

Step (3) 2D to 3D mapping →Raw 3D IR thermal map

Viewing angle distribution for the 3D surface

Correction formula for viewing angle artifacts

Step (4) 3D IR thermal map with corrected temperature

Figure 10 Flowchart with image data generated at each step leading to the accurate 3D IR thermal map with viewing angle artifact correction.
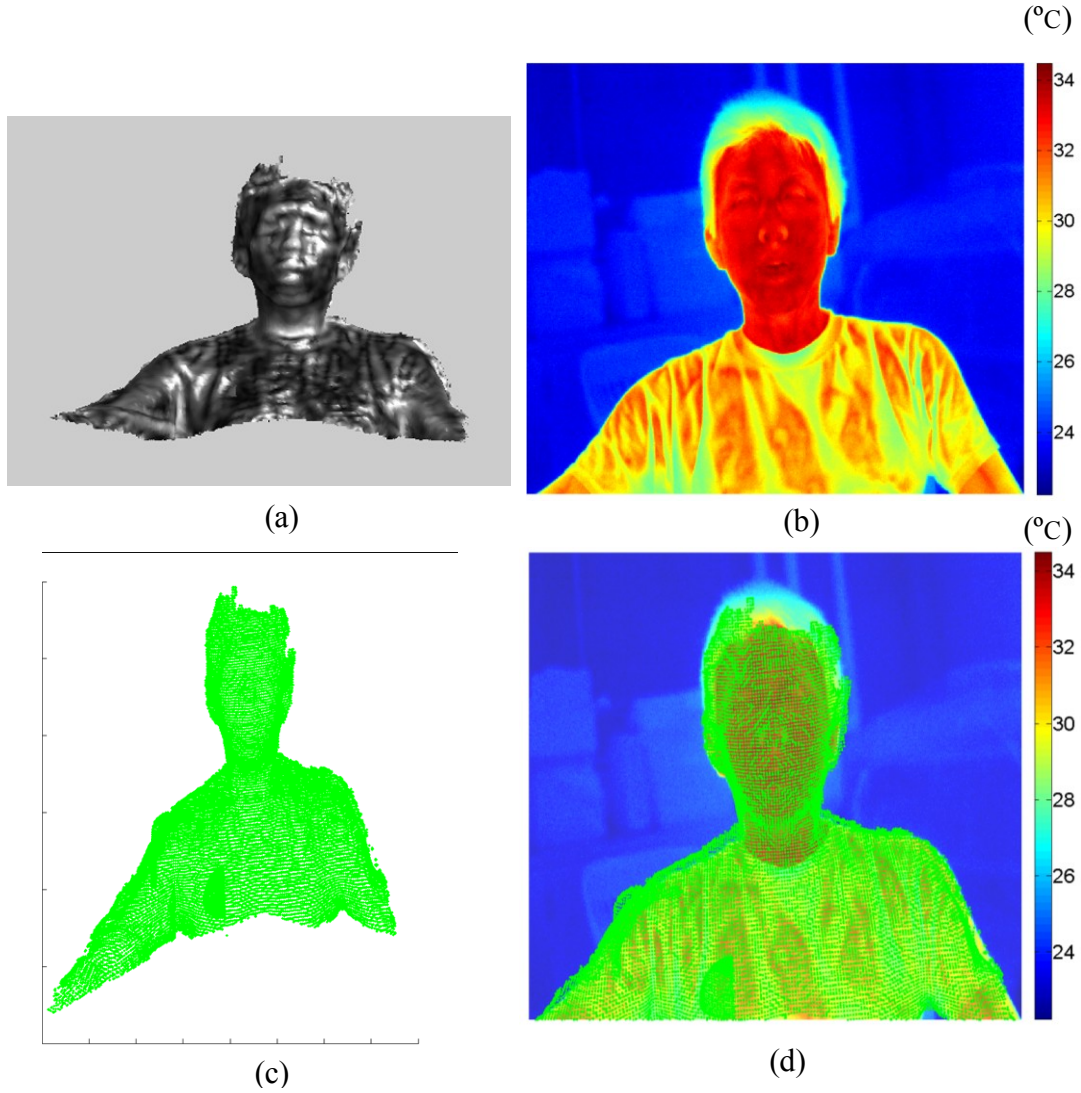
Figure 11 (a) 3D surface of human body captured by Kinect and reconstructed using ReconstructMe. (b) Color coded 2D thermal map acquired by the IR camera. (c) 2D projection of the reconstructed 3D surface grid in IR image coordinates. (d) Overlay of the 2D IR thermal map from (a) and the 2D projection of surface grid (green dots) from (c).

3.3 Reconstruction of the 3D IR image

To achieve the 2D-3D transformation demonstrated in the flowchart shown in Fig. 10, for each point on the reconstructed 3D surface grid, we determine the corresponding temperature by interpolation using the neighboring pixels in the IR image (Fig. 11(d)). The interpolated temperature value is then back-mapped to the point on the 3D grid, leading to the raw 3D IR thermal map displayed in Fig. 12.
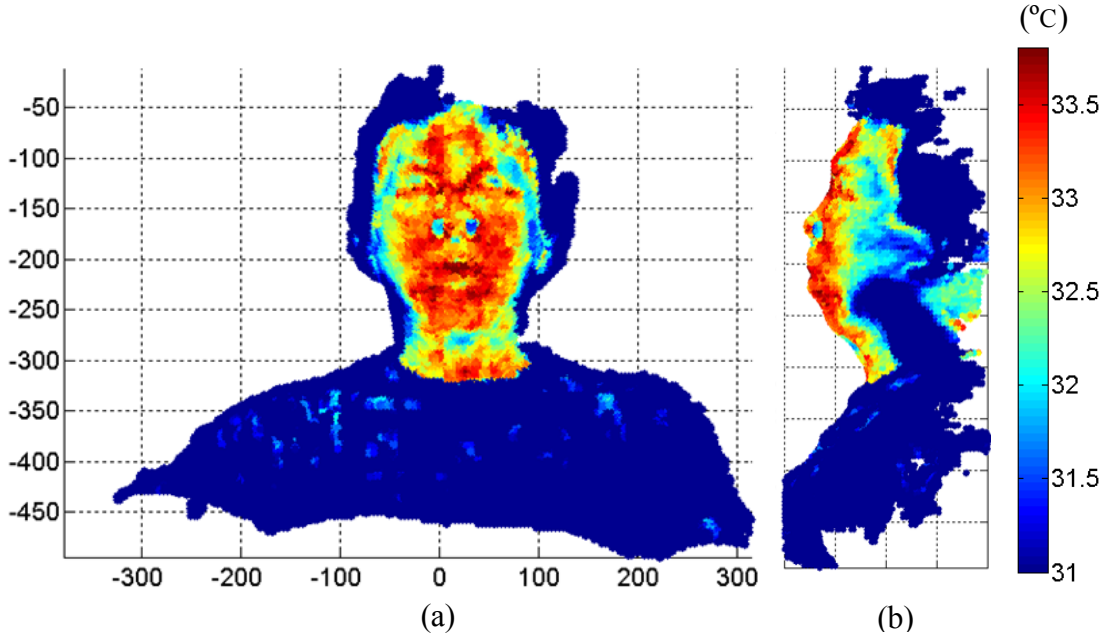
Figure 12 Raw 3D IR thermal map achieved by back-mapping the interpolated temperature from the 2D IR image to the 3D reconstructed surface: (a) front view and (b) side view.

In the side view of the raw 3D IR thermal map in Fig. 12(b), we can observe a dramatic decrease of temperature on the left cheek (in reality the cheek surface temperature exhibits much less temperature variation), where the viewing angle is clearly larger than 70° with respect to the IR camera axis. The temperature measurement is degraded due to the artifact of directional emissivity.

3.4 Computing the viewing angle for curvature artifact correction

In Step 4 in Fig. 10, the viewing angle distribution over the reconstructed 3D surface is computed using Eq. (28), and the result is presented in Fig. 13. Using the data for the 3D distribution of the viewing angle, the three directional emissivity correction formulas were applied to the raw 3D IR thermal map, resulting in three accurate 3D IR thermal maps displayed in Fig. 15.

As discussed in Section 2.6.4, in addition to the viewing angle of object, the correction effect depends on the directional emissivity model used. In our experiment the raw 3D IR thermal map is corrected using the three models introduced in Section 2.6.1, the dielectric model [45], the non-dielectric [54], and the cosine model. Results for these three models are displayed in Figs. 14(a),(b), Figs. 14(c),(d), and Figs. 14(e),(f), respectively. When applying correction formula, the room temperature of 23℃ was used as the ambient temperature T_a in Eq. (25). The temperature at the location with the viewing angle close to 0° (red arrow in Fig. 13), was taken as the $T_s(\theta = 0)$ in Eq.(26).
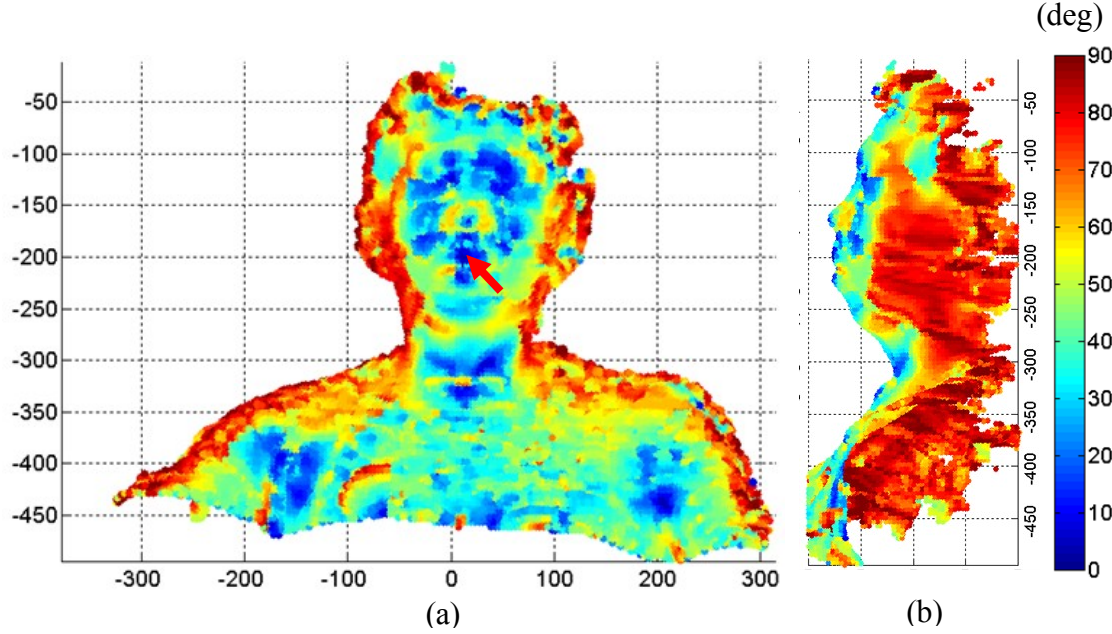
Figure 13 Viewing angle distribution of the reconstructed 3D surface computed by Eq.(28). The red arrow indicates the location with a viewing angle close to $0°$, the temperature at this location is used as the denominator: $T_s(\theta = 0)$ in Eq.(26) to determine the calibration coefficient S.

The three sets of corrected 3D thermal maps in Fig. 14 allow us to compare the correction effects generated by the three directional emissivity models. We can observe that in regions with large viewing angles, such as the cheeks, the temperature decreases dramatically in the raw 3D thermal map, as shown in Fig.12. The temperature in these regions is effectively recovered in Figs. 14(a),(b) (dielectric model) and Figs. 14(c),(d) (non-dielectric model). We can also observe that the temperature of the skin corrected by these two models becomes more uniform than the uncorrected distribution (Fig. 12). By comparing Figs. 14(a),(b) with Figs. 14(c),(d), we can conclude that the skin temperature is slightly higher for the non-dielectric model in regions with larger viewing angles (side view). This suggests that the non-dielectric model yields a slightly stronger temperature compensation than the dielectric model. The skin temperature corrected by cosine model, however, is clearly over-compensated, as illustrated in Figs. 14(e),(f), and the facial features even lose the original thermal contrast in the corrected 3D thermal map. The result implies that the cosine function is not a suitable model to describe the directional behavior of skin emissivity. The use of the cosine model may be appropriate in some engineering applications when directional emissivity data are unavailable, however, better models are available for skin properties in medical applications.

To further improve the accuracy of 3D thermal mapping of the human body for medical applications, a systematic experimental study of the directional emissivity would be essential, to validate existing models and develop better models. This study should measure directional emissivity for different skin types and evaluate the influence of factors such as age, hydration level, etc. on the directional emissivity of the human skin.
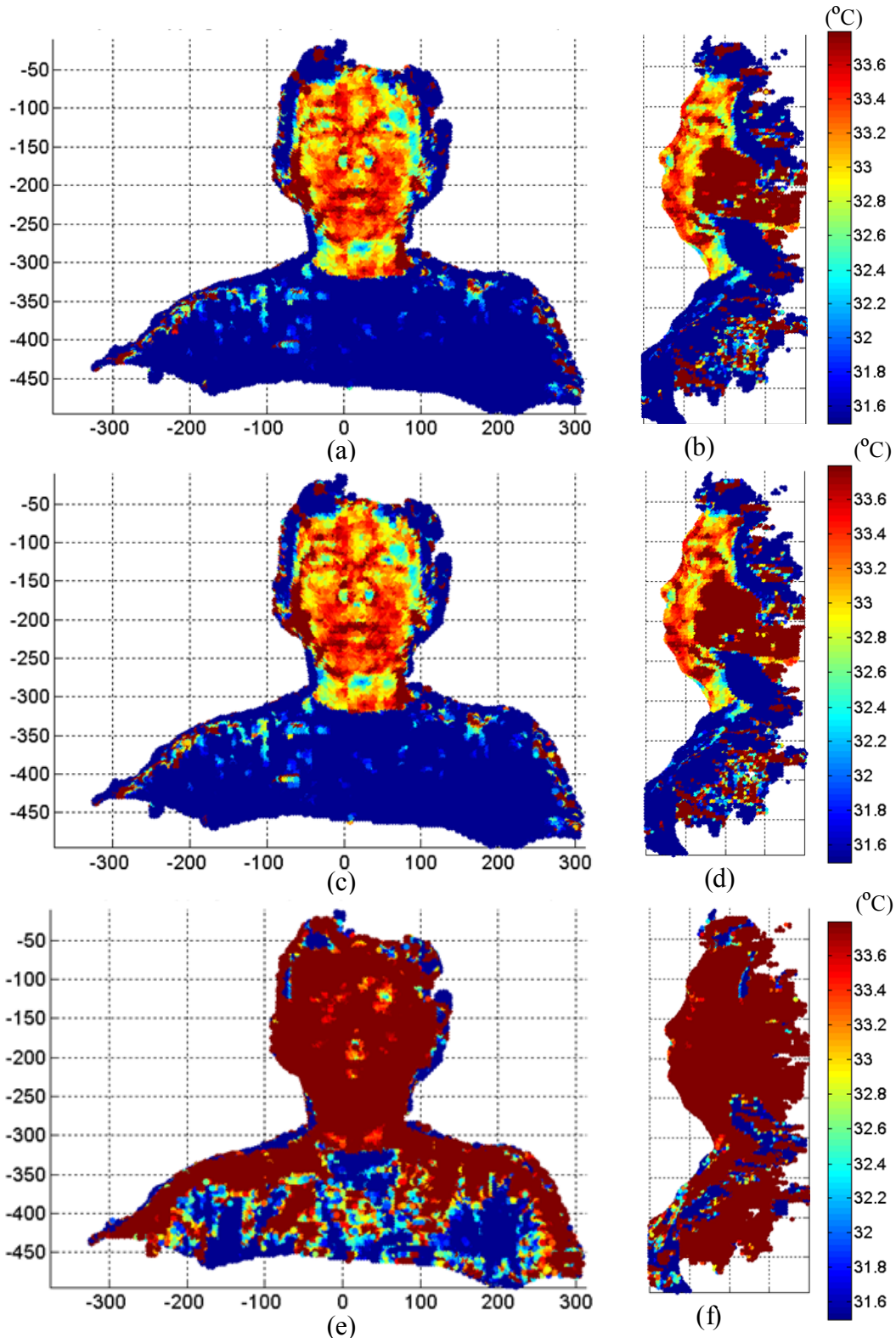
Figure 14 Front view (a) and side view (b) of 3D thermal map corrected by the dielectric model. Front view (c) and side view (d) corrected by the non-dielectric model and the front view (e) and side view (f) for the cosine model.

To evaluate the correction effects quantitatively, we selectively projected the corrected temperature of the face from the 3D space back into 2D image coordinates. The results of back-projection without correction, results corrected by the dielectric model (Figs. 14(a),(b)), and the non-dielectric model (Figs. 14(c),(d)) are shown in Figs. 15(a),(c) and (e), respectively. In the back-projection, temperature profiles along two horizontal lines across the face are shown in Figs. 15(b) and (d), where Fig. 15(b) illustrates temperature along the line crossing the forehead region (blue line in Figs. 15(a),(c),(e)). Fig. 15(d) displays temperatures along the line crossing the nose and two cheeks (green line in Figs. 15(a),(c),(e)).

The dashed line in Figs. 15(b) and (d) shows results without correction, and we can observe the pronounced decrease of temperature toward the two ends of the profile, as the surface of cheek region gradually points away from the camera axis. Conversely, the in profiles corrected by the dielectric and non-dielectric models (the solid and solid-dot lines in Figs. 15(b) and (d)), the temperature is more uniform toward the two ends of the profile. The temperature profile corrected by the non-dielectric model shows a stronger compensation. By subtracting the temperature profile of the uncorrected case (the dashed line in Figs. 15(b) and (d)) from the two corrected profiles (the solid and solid-dot lines in Figs. 15(b) and (d)), the temperature difference generated by the correction formula using the two models is contrasted in Fig. 15(f). We can observe that at the location with higher viewing angles (nose and temple regions), the temperature compensation provided by the correction formula is more significant. The magnitude of temperature compensation along the two lines is in the range of 0.2-1.4 $^{\circ}$C.

Finally, to evaluate the validity of the correction formulas, we acquired the 2D IR image for the side view (profile) of the subject's face as shown in Fig. 16(a). The left cheek in Fig. 16(a) was facing the IR camera, and thus the temperature distribution of the cheek can be scanned without the interference of the viewing angle artifact. For comparison (with Fig. 16(a)), the side views of the reconstructed 3D IR thermal maps before and after applying the correction (Fig. 12(b), Fig. 14(b) and Fig. 14(d)), are also displayed in Figs. 16(b)-(d). When compared with the uncorrected 3D IR thermal map (Fig. 16(b)), we can observe that the temperature distributions corrected either by the dielectric (Fig. 16(c)) or non-dielectric models (Fig. 16(d)) exhibit features more similar to the 2D IR image in Fig. 16(a). Particularly in the region of the temples and the jaw in Fig. 16(a) we can find that some hot spots originally degraded by the viewing angle artifact in Fig. 16(b), were recovered and become visually identifiable in Figs. 16(c) and (d). Therefore, the proposed four-step correction formula using the dielectric and non-dielectric models does improve the quantitative accuracy of 3D thermal mapping.
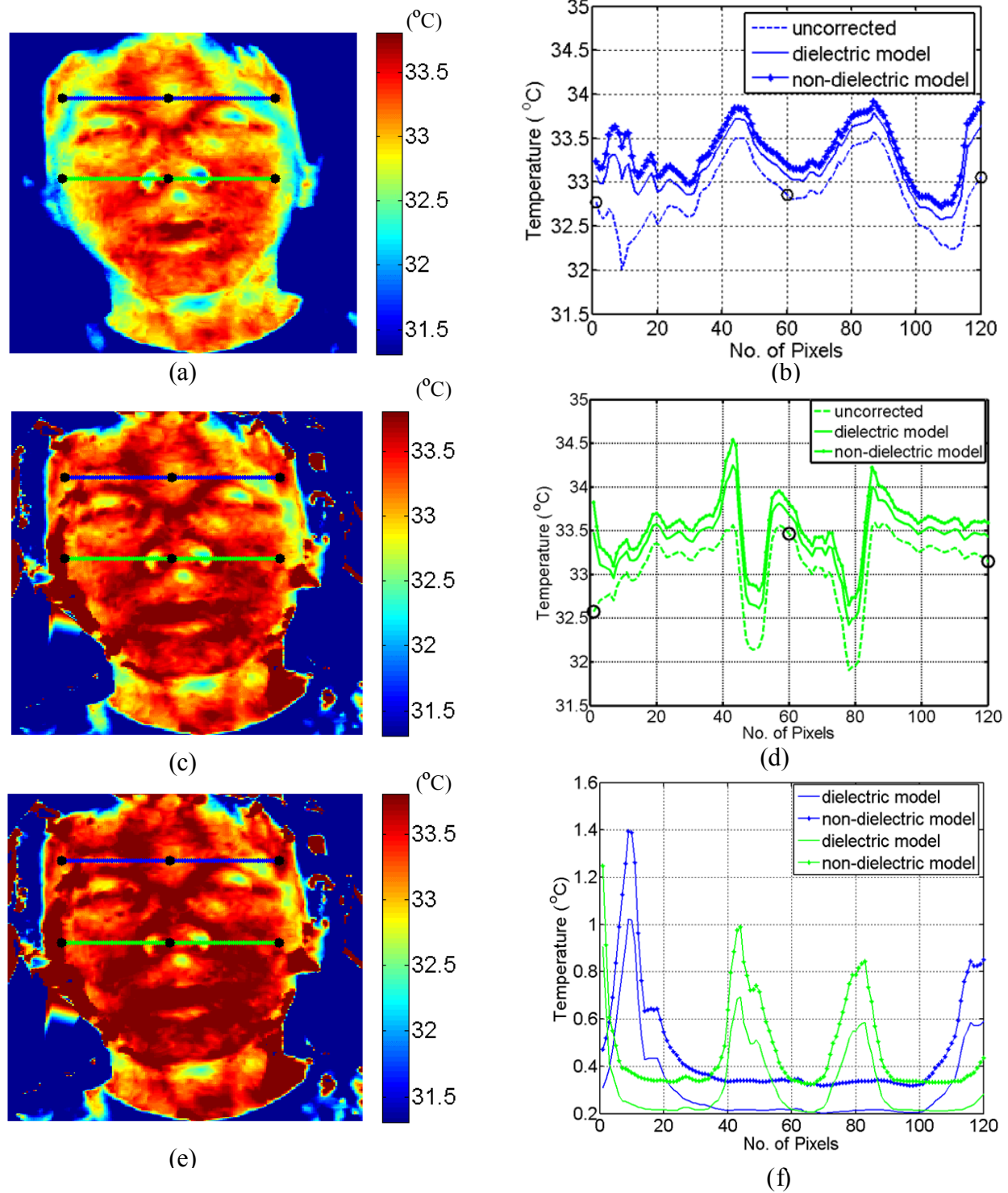
Figure 15 (Left): 2D projection of the 3D thermal map of the face: (a) without correction, (c) correction using dielectric model and the (e) non-dielectric model. **(Right)**: (b) Temperature profiles along the blue lines shown in (a)(c)(e). (d) Temperature profiles along the green line shown in (a)(c)(e). (f) Temperature difference between the corrected profiles and the uncorrected profile (subtracting the dashed line from the solid and solid-dot lines in (b) and (d)).
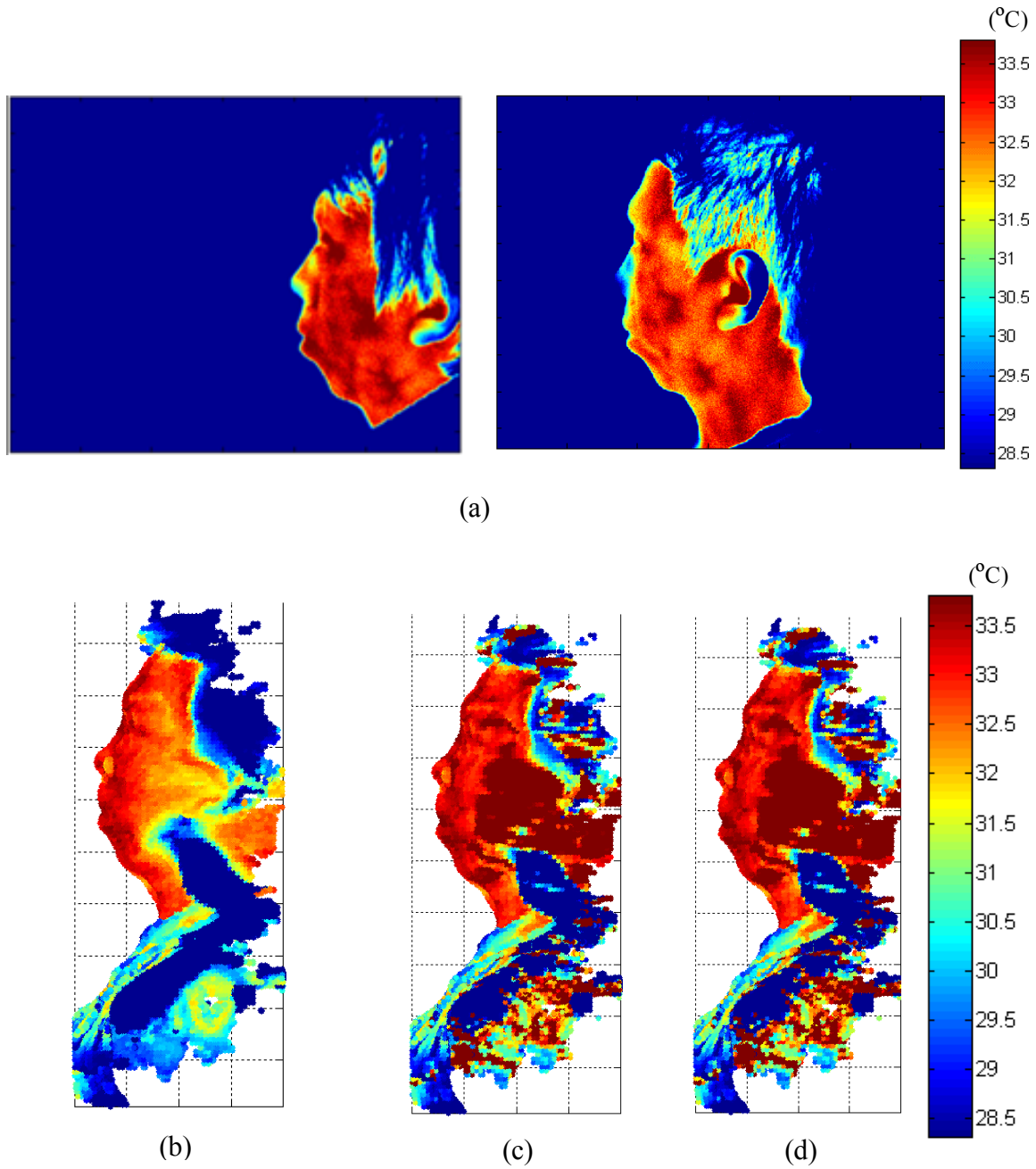
Figure 16 (a) 2D IR image of the side view of face. The image was acquired with the cheek facing the IR camera. (b) Side view of the raw (uncorrected) 3D IR thermal map. Side view of the 3D IR thermal map corrected by the (c) dielectric model and (d) the non-dielectric model.

4. Discussion and conclusions

In this paper, we successfully implemented 3D imaging of the human body by integrating the functionalities of the Microsoft Kinect 3D imager and the IR camera. This off-the-shelf hardware, combined with custom-developed and open-source software, serves as a low-cost platform for

clinical imaging applications. The resulting 3D thermal images of the skin combine the 3D spatial locations of the body surface with the corresponding temperature texture. The results reveal that the 3D imager of the Kinect, that uses structured light, yields reasonable reconstruction accuracy for 3D skin temperature measurements. Intrinsic and external camera parameters obtained from the checkerboard calibration [50, 51] were employed to project the 3D surface grid to the IR image coordinates. The successful mapping of the thermal texture onto the reconstructed 3D depth map of the face demonstrates the validity of the calibration method introduced by Herrera et al. [50, 51].

Using optical properties of pure water, in Section 2.6.3 we validated the theoretical predictions of the directional emissivity of skin using the dielectric and non-dielectric models. This allows us to correct for the systematic errors arising in temperature measurements of the skin when a significant surface curvature is present. However, the liquid contained in skin tissue is actually a saline solution rather than pure water, which may lead to differences in the optical and radiative properties. The optical and radiative properties of saline solutions in the infrared domain of the spectrum are not well known and would require further study. Furthermore, the models used in this study neglect the heterogeneous composition of material and scattering properties of surface, and a more accurate and complete model would have to account for these as well. To model the directional emissivity of skin with better fidelity, more fundamental studies are necessary to account for the identified in this section.

The validation conducted using the cylindrical phantom (Fig.9) demonstrates the feasibility of the correction algorithm proposed in this study. Therefore, given the viewing angle distribution as well as the 2D IR temperature map of the human body, the correction can be applied to estimate the measurement errors caused by the directional emissivity. More importantly, the systematic errors owing to the surface curvature can be corrected for, leading to an accurate temperature measurement.

One of the key challenges in quantitative medical diagnostic applications of IR thermography is the relatively large systematic measurement error (it can be of the order of 3-4°C, depending on the viewing angle and experimental conditions) introduced by applying flat plate blackbody calibration results to IR images of curved surfaces. The 3D surface map generated by the Kinect imager provides the information necessary to correct for artifacts appearing on curved surfaces due to the directional properties of surface emissivity. The viewing angle distribution over the body surface is computed from the surface normal vector orientation for the reconstructed 3D surface grid relative to the camera axis. A four-step approach to correct the viewing angle artifact is then applied to yield the 3D temperature distributions. According to the visual comparison of the 3D temperature distributions generated by 3D IR thermal map before and after correction, we can observe the skin region influenced by the directional emissivity artifact is reduced. In the corrected images the temperature changes more smoothly toward the regions with larger viewing angles. The resulting temperature patterns display higher similarity to the artifact-free temperature pattern in the 2D IR scan of the profile than those from uncorrected IR thermal map.

Due to incomplete data on the lateral side of a single 2D IR frontal image of the face, in some cases the temperature at a lateral location, such as the ear, is not reconstructed fully in 3D IR thermal map. In addition, since the temperature texture on the 3D surface is computed by interpolation based on 2D IR image data, the spatial reconstruction accuracy is limited by the spatial resolution of the IR camera. The spatial resolution of temperature measurements

decreases with increasing viewing angle as a larger surface area is covered per pixel at larger viewing angles. Thus, the resolution of 3D thermal map will improve when a 2D IR image with higher spatial resolution is used for reconstruction. The rapid development of IR technology holds the promise that high-resolution IR imagers will be available on the market at a reasonable cost in the near future. Furthermore, the foreseeable improvement of 3D depth resolution delivered by the new generation of Kinect devices will improve the accuracy of viewing angle mapping, leading to a more accurate correction and improved thermal map.

The inaccuracy caused by the incomplete projection can be improved by scanning multiple views of the human body. This allows the merging of different 3D depth profiles and 2D IR views into a complete 3D IR reconstruction. Multiple orientations provided by the multiple views can also be used for mutual calibration of the correction formula: temperature measured at the location with large viewing angle in one view, can be calibrated by its corresponding value in another view. The reference value used in the calibration is measured at a location facing the camera with zero viewing angle.

The designed imaging hardware system, which consists of one Kinect device and one IR camera, only needs to be calibrated once, and then the camera parameters obtained are reusable in subsequent measurements. The portability of the system also makes it suitable for the clinical environment. The convenience and the affordability of the system designed in this study makes it a promising solution to enable 3D IR thermographic imaging in medical as well as industrial applications.

References

[1] T.M. Button, H. Li, P. Fisher, R. Rosenblatt, K. Dulaimy, S. Li, B. O'Hea, M. Salvitti, V. Geronimo, C. Geronimo, S. Jambawalikar, P. Carvelli, R. Weiss, Dynamic infrared imaging for the detection of malignancy, Phys. Med. Biol., 49 (2004) 3105-3116.

[2] M.P. Cetingul, C. Herman, A heat transfer model of skin tissue for the detection of lesions: sensitivity analysis, Phys. Med. Biol., 55 (2010) 5933-5951.

[3] M.P. Cetingul, H.E. Cetingul, C. Herman, Analysis of transient thermal images to distinguish melanoma from dysplastic nevi, in: Proceedings of SPIE Medical Imaging 2011: Computer-Aided Diagnosis, 2011.

[4] M.P. Cetingul, C. Herman, Quantification of the thermal signature of a melanoma lesion, Int. J. Therm. Sci., 50 (2011) 421-431.

[5] M.P. Cetingul, C. Herman, The assessment of melanoma risk using the dynamic infrared imaging technique, J. Thermal Sci. Eng. Appl., 3(3) (2011) 031006.

[6] C. Herman, M.P. Cetingul, Quantitative visualization and detection of skin cancer using dynamic thermal imaging, J. Vis. Exp., (2011).

[7] C. Herman, Emerging technologies for the detection of melanoma: achieving better outcomes, Clin. Cosmet. Investig. Dermatol., 5 (2012) 195-212.

[8] C. Herman, The role of dynamic infrared imaging in melanoma diagnosis, Expert Rev. Dermatol., 8 (2013) 177-184.

[9] M. Gautherie, Thermobiological assessment of benign and malignant breast diseases, Am. J. Obstet. Gynecol., 147 (1983) 861-869.

[10] A.J. Collins, E.F.J. Ring, J.A. Cosh, P.A. Bacon, Quantitation of thermography in arthritis using multi-isothermal analysis .1. Thermographic index, Ann Rheum Dis, 33 (1974) 113-&.

[11] P. Aksenov, I. Clark, D. Grant, A. Inman, L. Vartikovski, J.-c. Nebel, 3D thermography for quantification of heat generation resulting from inflammation in: 8th 3D modelling symposium, Paris, France, 2003.

[12] X.Y. Ju, J.C. Nebel, J.P. Siebert, 3D thermography imaging standardization technique for inflammation diagnosis, in: Proceedings of SPIE Infrared Components and Their Applications, 2005, pp. 266-273.

[13] E.B. Silberstein, G.K. Bahr, J. Kattan, Thermographically measured normal skin temperature asymmetry in the human male, Cancer, 36 (1975) 1506-1510.

[14] L.J. Jiang, E.Y. Ng, A.C. Yeo, S. Wu, F. Pan, W.Y. Yau, J.H. Chen, Y. Yang, A perspective on medical infrared imaging, J. Med. Eng. Technol., 29 (2005) 257-267.

[15] D.A. Kennedy, T. Lee, D. Seely, A comparative review of thermography as a breast cancer screening technique, Integr Cancer Ther, 8 (2009) 9-16.

[16] R.S. Handley, The temperature of breast tumors as a possible guide to prognosis, Acta Unio. Int. Contra. Cancrum., 18 (1962).

[17] M. Gautherie, C.M. Gros, Breast thermography and cancer risk prediction, Cancer, 45 (1980) 51-56.

[18] D.J. Watmough, P.W. Fowler, R. Oliver, The thermal scanning of a curved isothermal surface: implications for clinical thermography, Phys Med Biol, 15 (1970) 1-8.

[19] J.A. Clark, Effects of surface emissivity and viewing angle errors in thermography, Acta thermographica, 1 (1976) 138-141.

[20] C.J. Martin, D.J. Watmough, Thermal scanning of curved surfaces, Acta thermographica, 2 (1977) 18-22.

[21] R.E. Woodrough, Medical Infra-red Thermography: Principles and Practice, Cambridge: Cambridge University Press, 1982.

[22] C.J. Ash, E. Gotti, C.H. Haik, Thermography of the curved living skin surface, Mo Med, 84 (1987) 702-708.

[23] M. Anbar, Potential artifacts in infrared thermographic measurements, Thermology, 273 (1991) 3.

[24] S. Hejazi, R. Spangler, Theoretical Modeling of Skin Emissivity, P Ieee Embs, 14 (1992) 258-259.

[25] T.M. Buzug, S. Schumann, L. Pfaffmann, U. Reinhold, J. Ruhlmann, Skin-tumour classification with functional infrared imaging, Iasted Int Conf Sign, (2006) 313-322.

[26] M.P. Cetingul, H.E. Cetingul, C. Herman, Analysis of Transient Thermal Images to Distinguish Melanoma from Dysplastic Nevi, Proc Spie, 7963 (2011).

[27] C. Herman, The role of dynamic infrared imaging in melanoma diagnosis, Expert Rev Dermatol, 8 (2013) 177-184.

[28] TY. Cheng, C. Herman, Curvature effect quantification for in-vivo IR thermography, in: IMECE 2012, ASME International Mechanical Engineering Congress and Exposition, Houston, Texas, 2012.

[29] G. Sansoni, M. Trebeschi, F. Docchio, State-of-the-art and applications of 3D imaging sensors in industry, cultural heritage, medicine, and criminal investigation, Sensors, 9 (2009) 568-601.

[30] K. Khoshelham, S.O. Elberink, Accuracy and resolution of kinect depth data for indoor mapping applications, Sensors, 12 (2012) 1437-1454.

[31] P. Henry, M. Krainin, E. Herbst, X.F. Ren, D. Fox, RGB-D mapping: Using Kinect-style depth cameras for dense 3D modeling of indoor environments, Int J Robot Res, 31 (2012) 647-663.

[32] V. Hilsenstein, Surface reconstruction of water waves using thermographic stereo imaging, in: Proceedings of Image and Vision Computing New Zealand, Dunedin, New Zealand, 2005, pp. 102-107.

[33] Y.H.Ng, R.Du, Acquisition of 3D surface temperature distribution of a car body, in: Proceedings of IEEE International Conference on Information Acquisition, Hongkong, 2005, pp. 16-20.

[34] C. Rocchini, P. Cignoni, C. Montani, P. Pingi, R. Scopigno, A low cost 3D scanner based on structured light, Comput Graph Forum, 20 (2001) C299-+.

[35] L. Ciupitu, A.N. Ivanescu, S. Chivescu, S. Brotac, Vision system for human body infrared thermography, in: Annals of Daaam for 2009 & Proceedings of the 20th International Daaam Symposium, 2009, pp. 1545-1546.

[36] R.Q. Yang, Y.Z. Chen, Design of a 3-D infrared imaging system using structured light, Ieee T Instrum Meas, 60 (2011) 608-617.

[37] I. Grubisic, L. Gjenero, T. Lipic, I. Sovic, T. Skala, Medical 3D thermography system, Periodicum Biologorum, 113 (2011) 401-406.

[38] J. Shotton, T. Sharp, A. Kipman, A. Fitzgibbon, M. Finocchio, A. Blake, M. Cook, R. Moore, Real-time human pose recognition in parts from single depth images, Communications of the Acm, 56 (2013) 116-124.

[39] K. Skala, T. Lipic, I. Sovic, L. Gjenero, I. Grubisic, 4D thermal imaging system for medical applications, Periodicum Biologorum, 113 (2011) 407-416.

[40] H.P. Oliveira, P. Patete, G. Baroni, J.S. Cardoso, Development of a BCCT quantitative 3D evaluation system through low-cost solutions, in: Proceedings of the 2nd International Conference on 3D body Scanning Technologies, Lugano, Switzerland, 2011, pp. 16-27.

[41] G. Lu, G.N. DeSouza, J. Armer, B. Anderson, C.-R. Shyu, A system for limb-volume measurement using 3D models from an infrared depth sensor, in: Computational Intelligence in Healthcare and e-health (CICARE), 2013 IEEE Symposium on, Singapore, 2013, pp. 64-69.

[42] G. Cardone, A. Ianiro, G. dello Ioio, A. Passaro, Temperature maps measurements on 3D surfaces with infrared thermography, Exp Fluids, 52 (2012) 375-385.

[43] S. Colantonio, M. Benvenuti, M.G. Di Bono, G. Pieri, O. Salvetti, Object tracking in a stereo and infrared vision system, Infrared Phys. Technol., 49 (2007) 266-271.

[44] in, Official website of ReconstructMe (PROFACTOR)

http://reconstructme.net/, 2015.

[45] D.J. Watmough, P.W. Fowler, R. Oliver, The thermal scanning of a curved isothermal surface: implications for clinical thermography, Phys. Med. Biol., 15 (1970) 1-8.

[46] B.F. Jones, A reappraisal of the use of infrared thermal image analysis in medicine, Ieee T Med Imaging, 17 (1998) 1019-1027.

[47] J. Steketee, Spectral emissivity of skin and pericardium, Phys. Med. Biol., 18 (1973) 686-694.

[48] T.M. Buzug, S. Schumann, L. Pfaffmann, U. Reinhold, J. Ruhlmann, Skin-tumour classification with functional infrared imaging, in: Proceedings of the Eighth IASTED International Conference on Signal and Image Processing, 2006, pp. 313-322.

[49] A. Bhargava, A. Chanmugam, C. Herman, Heat transfer model for deep tissue injury: a step towards an early thermographic diagnostic capability, Diagn. Pathol., 9 (2014) 36.

[50] C.D. Herrera, J. Kannala, J. Heikkila, Joint depth and color camera calibration with distortion correction, Ieee T Pattern Anal, 34 (2012) 2058-2064.

[51] C.D. Herrera, Kinect Calibration Toolbox, in, http://www.ee.oulu.fi/~dherrera/kinect/, 2012.

[52] J. Heikkila, Geometric camera calibration using circular control points, Ieee T Pattern Anal, 22 (2000) 1066-1077.

[53] R. Hartley, A. Zisserman, Multiple View Geometry in Computer Vision, 2 ed., Cambridge University Press, 2004.

[54] S. Hejazi, R. Spangler, Theoretical modeling of skin emissivity, in: P Ieee Embs, 1992, pp. 258-259.

[55] R. Siegel, J.R. Howell, Thermal Radiation Heat Transfer, 3 ed., Taylor & Francis Inc, Hemisphere, Washington, 1992.

[56] M.E. Thomas, Optical Propagation in Liquids in: Optical Propagation in Linear Media Oxford University Press 2006 pp. 423-442

[57] M.E. Thomas, Applied Physics Laboratory at Johns Hopkins University, 2015.

[58] M.R. Querry, D.M. Wieliczka, D.J. Segelstein, Handbook of Optical Constants of Solids II, Academic Press, San Diego, 1991.

[59] Emissivity Coefficients of some common Materials, http://www.engineeringtoolbox.com/emissivity-coefficients-d_447.html.

[60] S. Nakamura, M. Saito, L.F. Huang, M. Miyagi, K. Wada, Infrared optical-constants of anodic alumina films with micropore arrays, Jpn J Appl Phys 1, 31 (1992) 3589-3593.